

Wideband Feeding Network Design For Dual-Polarized Connected Arrays

by

Zhuang Chen

Committee: Prof. dr. A. Neto, TU Delft, Professor, Chairman
Dr. D. Cavallo, TU Delft, Associate Professor, Daily supervisor
Prof.dr. A. Freni, University of Florence, Associate Professor

Preface

Abstract

Phased arrays have emerged as a key solution for 5G base stations, to provide higher capacity by means of directive and electronically steerable beams. However, the implementation of workable low-cost antenna arrays for base stations is very challenging, because of the requirements on the total frequency and angular coverage of 5G systems. When many frequency bands are used for different services, having a single narrowband antenna for each sub-band becomes unfeasible for cost and space occupation. For this reason the use of wideband arrays that can cover simultaneously multiple bands is gaining interest. Moreover, a large field of view is required, i.e. scanning at least from -60° to $+60^\circ$, so that only a few array panels can cover the entire azimuthal angle of 360° .

This thesis work has been performed in the framework of a collaboration between Terahertz Sensing Group and HUAWEI, aiming at the development of a wideband phased array for base station applications. Two array designs are targeted, one covering the band 6-8 GHz and another operating in the band 2-8 GHz. Both designs are required to achieve wide scanning capability up to 60° in all azimuth planes. The specific focus of this thesis is on the design of the feeding structure of the array unit cell and the corporate feeding networks for the finite array.

The unit cell feeding structure is based on integrated coaxial lines connected to microstrips or striplines. The performance is analysed first for the stand-alone transition and then for the same feed together with the connected slot element. The total matching performance of the entire unit cell including the feed are shown to be comparable to the one of the ideal unit cell without feeding structure. An alternative feed design is also presented, where the input is realized with a coaxial SMP connector.

The design of a corporate feeding network for the array is introduced. This consists of two designs of 1-to-32 power dividers, one implemented with microstrip transmission lines and the other with striplines. Such dividers are meant to feed in phase an entire row or column of the array. The highlights of this design is wide bandwidth, which covers two octaves by means of wideband multi-section and tapered impedance transformers, and the compactness, since the entire divider has to fit in an area of $480 \text{ mm} \times 15 \text{ mm}$.

Moreover a novel feeding strategy is proposed to simplify the complexity and the costs of the unit cell. The new approach is based on replacing the coaxial lines with integrated parallel plate waveguides (PPW). Two examples of unit cell design, based on this new feed concept, are presented: one consists in a single-polarized array of connected slot, covering the band from 70 GHz to 140 GHz, for automotive radars; another example is referring to a dual-polarized connected slot array covering the same 2-8 GHz range, for wideband base stations. The design procedure of a PPW and cavity is easier than that of the integrated coaxial, as the feed and the radiating slot design are better decoupled. The number of layers of the ADL is also reduced with respect to the integrate coaxial, because part of the impedance transformation is implemented in the PPW.

Acknowledgement

First I would like to thank all the teachers in Terahertz Sensing Group for leading me into the field of electromagnetism where some parts are quite new to me. And I would like to thank my supervisor Daniele Cavallo for your patient instruction. Although being very busy, you were always able to have meetings with me every week to solve my problems and willing to teach me more about the nature of the design, which helped me a lot with the comprehension of theory. I am also willing to thank Riccardo Ozzola. As a PhD student, you were very kind and helpful. Although this is the first year you to supervise Master student, I have to say that you have done really well. We were always in connection during the whole thesis, and you were really professional and patient in guiding me.

Zhuang Chen
August 2021

Contents

1	Introduction	1
1.1	Motivation	1
1.2	State of the Art	2
1.3	Antenna Concept	3
1.3.1	Connected Arrays	3
1.3.2	Artificial Dielectric Layers (ADLs)	4
1.4	Project Overview and Requirements	6
1.5	Outline of the Thesis	7
2	Array with Integrated Coaxial Feed	9
2.1	Integrated Coaxial Introduction	9
2.2	Unit Cell	10
2.3	32×32 Array with Integrated Coaxial Feed	11
2.3.1	Integrated Coaxial Feed	11
2.3.2	Unit Cell with Integrated Coaxial Feed	13
2.4	8×8 Array with Integrated Coaxial Feed	14
2.4.1	SMP Connector	14
2.4.2	Integrated Coaxial Feed with SMP Connectors and ADL	15
2.5	Cross-Polarization Levels	16
2.6	Simulated Unit Cell Efficiency	18
3	Design of Wideband Corporate Feeding Network	19
3.1	Theoretical Background	19
3.1.1	T-junctions	19
3.1.2	Impedance Transformers	20
3.2	Corporate Feeding Network	24
3.2.1	Microstrip Feeding Network	25
3.2.2	Stripline Feeding Network	27
4	Parallel Plate Waveguide Feeding Structure	30
4.1	Novel Feed Concept	30
4.1.1	Drawbacks of Integrated Coaxial Feed	30
4.1.2	PPW Feed	31
4.2	Example: 70 to 140 GHz Linearly Polarized Array	32
4.2.1	Artificial Dielectric Design	32
4.2.2	Array Fed with a Straight PPW	33
4.2.3	Array Fed with a Folded PPW	34
4.2.4	Array Unit Cell with ADLs	35

4.3	Example: 2 to 8 GHz Array	36
4.3.1	Artificial Dielectric Design.	36
4.3.2	Array Fed with a Straight PPW	37
4.3.3	Array Fed with a Folded PPW	40
4.3.4	Array with ADLs	40
4.4	Array for Dual Polarization.	41
5	Conclusions and Future Work	45
5.1	Conclusions	45
5.2	Future Work	46
A	Derivation of the Impedance for 5-Section Chebyshev Transformers	47
B	Prototype of the Final Board Design	49
B.1	Antenna Boards	49
B.2	Radome Boards	49
	Bibliography	54

Introduction

1.1. Motivation

Phased arrays have emerged as a key solution for 5G base stations, to provide a higher capacity by means of directive and electronically steerable beams. In the previous standards, a wide beam was used to cover simultaneously all the users located within the cell, but this approach is radically subverted in 5G with the use of massive multiple-input and multiple-output (MIMO). This is based on the possibility to transmit and receive multiple data streams through directive beams connecting the base station with different users [1–3]. Antenna arrays will focus the radiation in smaller angular regions with the aim to improve the energy and spectral efficiency, while reducing interference levels. Since the users can move, the antenna has to steer its beam over a wide Field of View (FoV) in order to track the user's movement, and to maintain the link active, as shown in Fig. 1.1(a). Thus, multi-beam phased array antennas are regarded as a key technology for enabling massive MIMO and high-speed mobile networks.

Besides the multi-beam capability, the 5G communication standard relies on the possibility of transmitting information over several bands of the electromagnetic spectrum. The development of the sub-6 GHz frequency range, also known as the golden band, is of paramount importance due to the favourable propagation conditions and due to the avail-

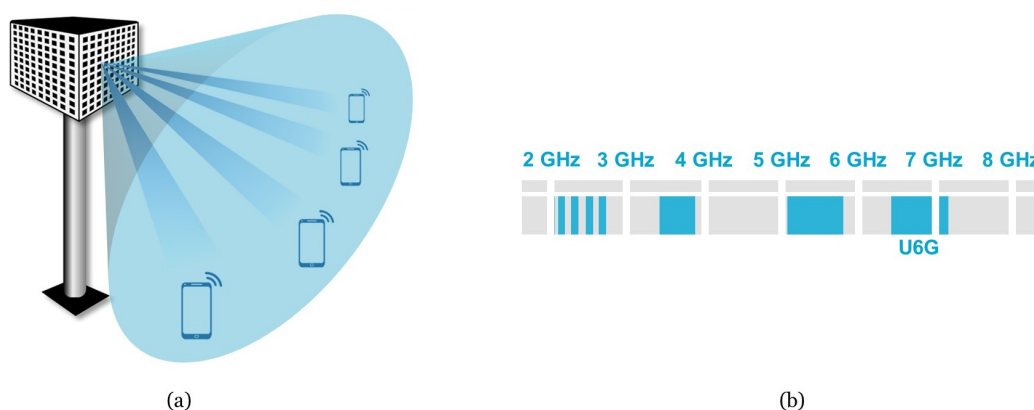


Figure 1.1: (a) 5G band allocation for the sub-6 GHz frequency range, including the U6G band; (b) Depiction of a massive MIMO base station antenna.

able bandwidth. Several bands have already been licensed between 2 and 8 GHz, one more band located between 6.425 and 7.125 GHz will be licensed in a few years [4], and more bands are expected to be standardized around this, as shown in Fig. 1.1(b). However, the resonant antennas, which are currently being employed in base stations, are characterized by narrowband properties, and can cover only one band at a time. By using this approach, several antennas are needed to cover all the required bands, leading to a high number of antennas competing for the same space or increasing the overall space occupied by the base station. It is then clear that the use of resonant antennas will soon become unsuited for wireless applications, as more and more bands are allocated to provide different services. To overcome this problem, the need of wideband wide-scanning phased arrays is emerging for base station antennas. Arrays with very wide frequency ranges can cover multiple 5G bands simultaneously and combine several functions/bands into a single shared radiating aperture.

This thesis is embedded in a research project aiming at designing a wideband phased array capable of covering the band between 2 and 8 GHz, thus reducing the number of antennas on the same base station platform. Wide angle capabilities will be targeted, allowing the main beam to scan between -60° and $+60^\circ$. Slant-linear polarized fields¹ are customarily used due to the favorable propagation conditions, so to radiate such fields a dual-polarized antenna is desired. The current trend for massive MIMO antennas is to increase the number of elements to maximize the number of independent data streams transmitted to the different users, and to reduce the power feeding each transmit/receive (T/R) module, allowing the use of low cost electronics. Thus very large planar arrays with 32×32 elements will be considered.

More specifically, the main focus of this thesis is on the design of the feeding structure of the array.

1.2. State of the Art

As stated in Sec. 1.1, narrowband antennas are commonly used for base stations [5–7]. However, due to the high number of in-use bands, numerous antennas are deployed, making either base stations grow in dimensions (leading to larger space occupation, higher rental, and maintenance costs), or antennas compete for the same space, as shown in Fig. 1.2.

For this reason the use of wideband arrays, with impedance matching response that covers multiple bands, is gaining interest [8, 9]. In the field of ultra-wideband array, two antenna solutions are the most typical choices to achieve multi-octave capability: tapered slot antennas (also known as Vivaldi antennas) [10–16] and connected arrays (also referred to as tightly coupled arrays) [17–25].

Typical implementation of dual-polarized Vivaldi arrays involves complex assembly of a set of vertical printed circuit boards (PCBs) intersecting in an egg-crate configuration. Tapered slots are characterized by large vertical dimension compared to the wavelength. The bandwidth of the array can be enlarged by increasing the length of the antenna elements, but elements pattern may suffer from scan blindness due to common-mode resonances propagating on the flared vertical edges [16]. Another drawback of this type of arrays is

¹In a slant polarization antenna, rather than horizontal and vertical, the polarization is at -45° and $+45^\circ$ from a reference plane of 0° .

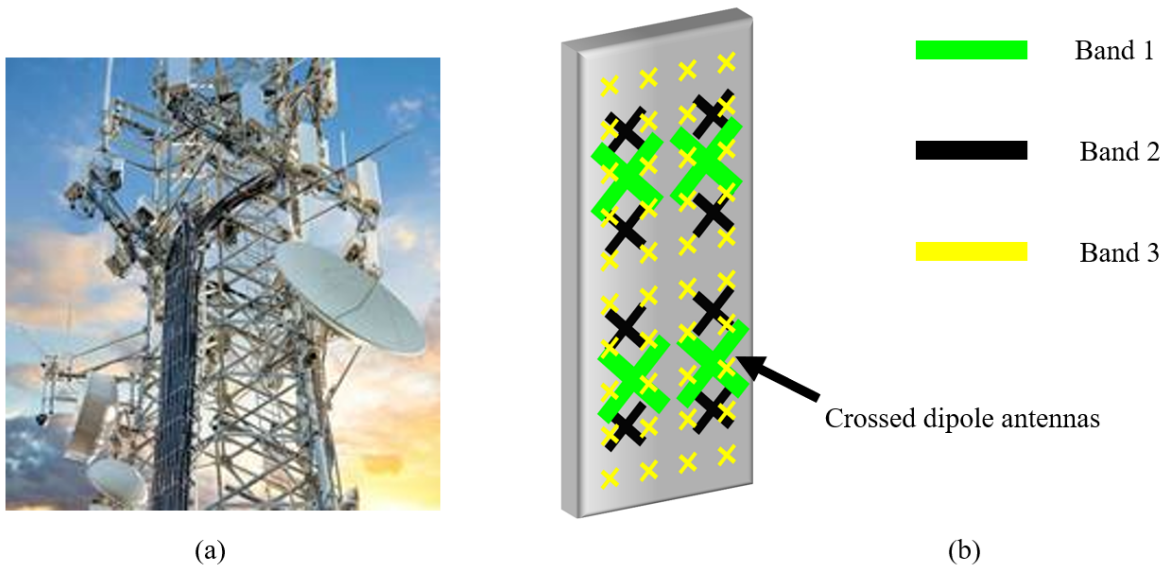


Figure 1.2: (a) Several resonant antennas for different bands in one base station and (b) typical sector antenna with several coexisting arrays operating in different bands.

the relatively high cross polarization when scanning in the diagonal planes [11, 26, 27]. The high cross-polar levels of the radiated field originate from the vertical component of the current distribution propagating on the flared edges of the tapered slot.

Connected arrays can achieve comparable bandwidth performance as Vivaldi, but allow for planar low-profile implementations. Tightly coupled arrays have been proposed recently for millimeter wave communication [8, 28, 29]. However, also for low frequency applications, below 10 GHz, wideband antennas are crucial to reduce the space occupied by the systems. In this thesis, connected arrays are considered as the antenna solution for the wideband array design.

1.3. Antenna Concept

1.3.1. Connected Arrays

Conventional narrowband array designs usually attempt to minimize the mutual coupling between elements. However in connected arrays the mutual coupling is intentionally increased to provide wideband operation [30]. Unlike resonant dipoles or slots in Fig. 1.3(a), connected arrays are obtained by electrically connecting the dipoles or slots as shown in Fig. 1.3(b). This results in long dipoles or long slots that are periodically fed. As the elements are connected, the current and field distributions are nearly constant with frequency, so that wideband properties are achieved.

Connected arrays are designed in the presence of a backing reflector to achieve unidirectional radiation. Since these arrays are characterized by a nearly uniform current distribution on the radiating aperture, they can be used to approximate a Wheeler current [31] and their input impedance is close to the one of free space, when scanning towards broadside in the presence of a backing reflector. However, each array element is typically fed by a transmission line with characteristic impedance Z_L , different from the characteristic

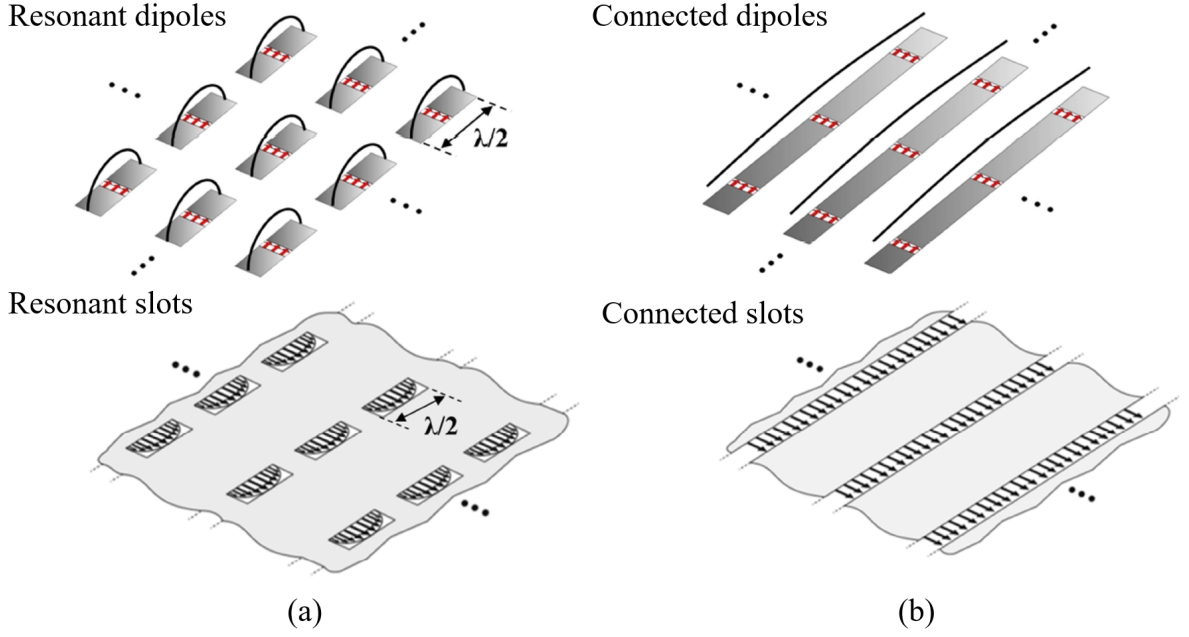


Figure 1.3: Electric current/field distributions on (a) arrays of resonant dipoles and slots and (b) arrays of connected dipoles and slots.

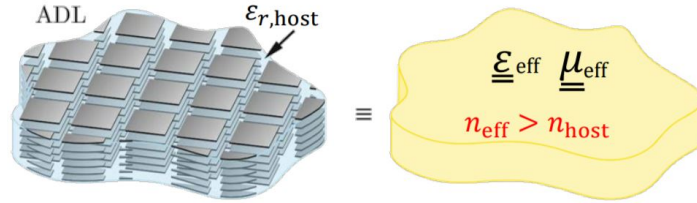


Figure 1.4: Artificial dielectric layers to realize an equivalent anisotropic material.

impedance of free space ζ_0 . An impedance transformer should be introduced to render a smoother transition between Z_L and ζ_0 , and thus reducing the mismatch. Such transformer can be realized using dielectric superstrates. However, the use of isotropic dielectric slabs will make the waves emanated from the feed with an incident angle above the critical angle face a total internal reflection and remain trapped in the dielectric. These waves are called surface waves and are not desired because they will cause power loss and reduce the antenna efficiency.

1.3.2. Artificial Dielectric Layers (ADLs)

The surface wave problem can be solved by using artificial dielectric layers (ADLs) with anisotropic properties above the connected array [32–35]. ADLs are sub-wavelength square metal patches, periodically arranged inside a host medium, as shown in Fig. 1.4. The presence of the metal inclusions results in an effective refractive index larger than the one of the host medium [36]. To obtain a set of desired effective parameters, one can change the permittivity of the dielectric spacer between the two metal layers, the gap between patches, the transverse period of the patches, the distance and shift between two adjacent layers. An angle-dependent effective refractive index is produced in ADLs, that is, the equivalent

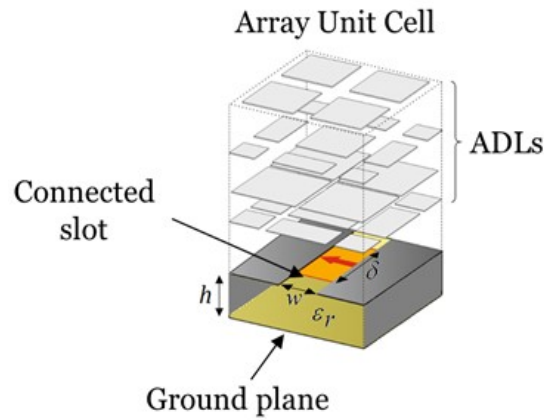


Figure 1.5: Sketch of the connected array unit cell with the ADL superstrates.

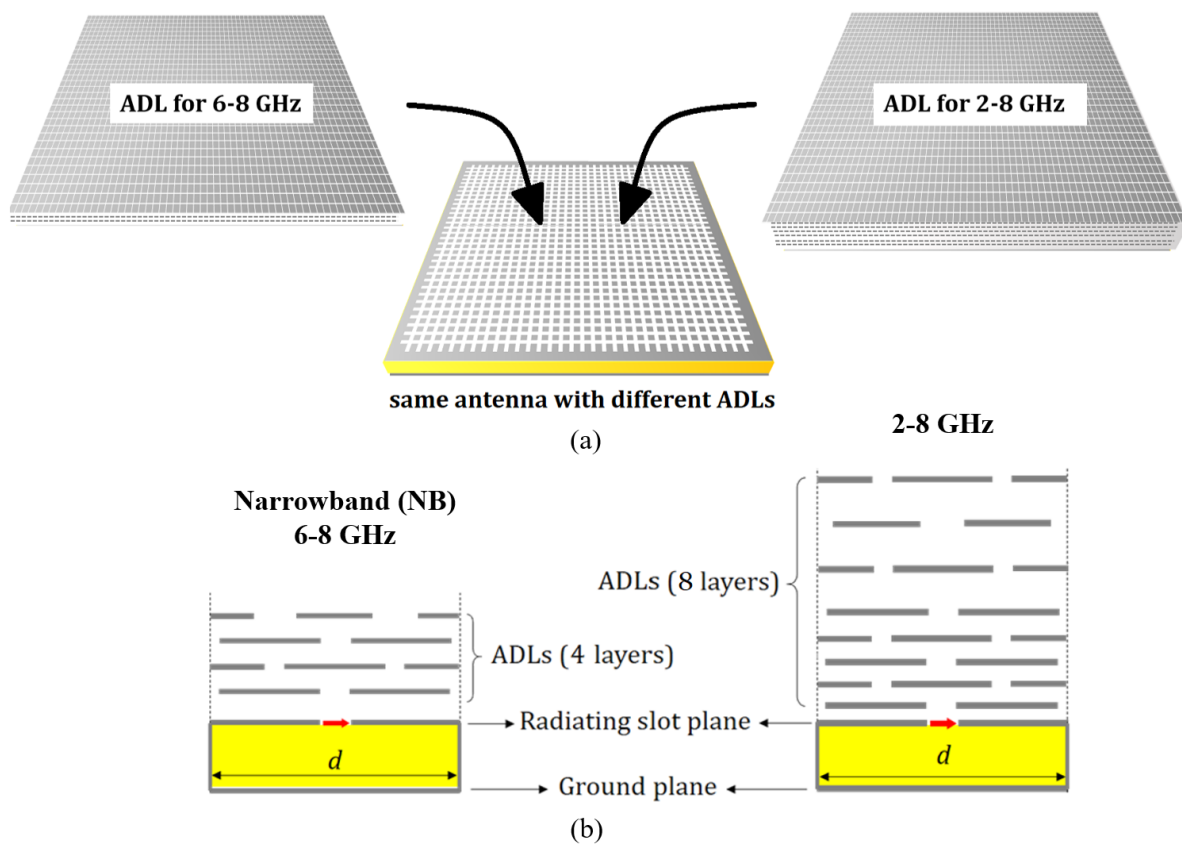


Figure 1.6: (a) 32×32 connected slots array with interchangeable ADL; (b) Stack up of the two structures.

permittivity decreases with the angle of incidence. This characteristic property allows the electromagnetic rays within the ADL slab to never encounter the critical angle, thus avoiding surface wave excitation.

Combining the connected array of slots with ADLs results in a typical unit cell as depicted in Fig. 1.5 [37, 38]. The radiating element is a connected slot excited with a delta gap generator and backed by a grounded slab. The slot ends touch the periodic boundary, thus the slot is connected to the neighboring elements. The resulting structure does

not support the typical resonant magnetic current of a half wavelength slot, but a uniform (wideband) current distribution. To compensate for the frequency dependence due to the distance to the backing reflector, ADLs are placed above the slot. ADLs also guarantee a high front-to-back ratio, while increasing the scanning range.

1.4. Project Overview and Requirements

This thesis work is embedded in the framework of a project with HUAWEI, aiming at developing a connected array prototype for base station applications. The designs of a first prototype covering from 6 to 8 GHz, referred to as narrowband (NB), and a second prototype covering from 2 to 8 GHz, indicated as wideband (WB), are targeted. However, instead of realizing two different designs, a single design of the dual polarized connected slot array is considered in combination with two interchangeable ADL slabs, one for the NB and the other for the WB operations, respectively. This approach can reduce the cost of the prototype and fully exploit the flexibility and the modularity of the structure. In this way, the frequency band of operation can be changed just by replacing the ADL radome, as shown in Fig. 1.6.

Regarding the number of antenna elements in the array, today's massive MIMO systems comprise relatively small antenna arrays, with 32 or 64 elements, and up to hundreds in some cases. However, for future base stations, the trend is to increase the number of elements in order of thousands, to reduce the amount of power for each T/R module. A larger number of elements is also important because it is proportional to the maximum number of simultaneous independent beams that can be realized with the phased array. For these reasons, a large prototype array, comprising $32 \times 32 \times 2 = 2048$ elements, is targeted in the project.

The connectorization of all elements is not advisable since a total of 2048 connectors would require an enormous number of measurements for the estimation of the active S-parameters. Moreover, the costs of 2048 coaxial connectors and 2048 50-Ohms terminations would be prohibitive. As an alternative solution, it is proposed to realize a hybrid approach, where for one polarization a corporate feeding network (1-to-32) feeds all the elements on the same slots, and for the other polarization another corporate feeding network feeds all the elements aligned across the slot, as shown in Fig. 1.7(a) and (b). This solution will result in a more manageable number of connectors (64 in total) and will allow at the same time to analyze scanning performance and multi-beam capability by the post-processing combination of the embedded radiation patterns associated with each feeding port. Since the two feeding networks for the orthogonal polarizations have to coexist in the same antenna stack-up, they will be realized in different metal layers, one based on microstrips and the other on striplines, separated by a ground plane to avoid coupling (Fig. 1.7(c)).

The feeding strategy described in Fig. 1.7(a) and (b) does not allow to measure the cross-polarization on the diagonal plane. For this reason an addition smaller version of the array will be also manufactured, with 8×8 elements, fully connectorized. This will allow to measure the cross-polarization of the central element when scanning in the diagonal plane (Fig. 1.8). In principle the cross-polarization of every element can be measured but we will measure the central one for convenience.

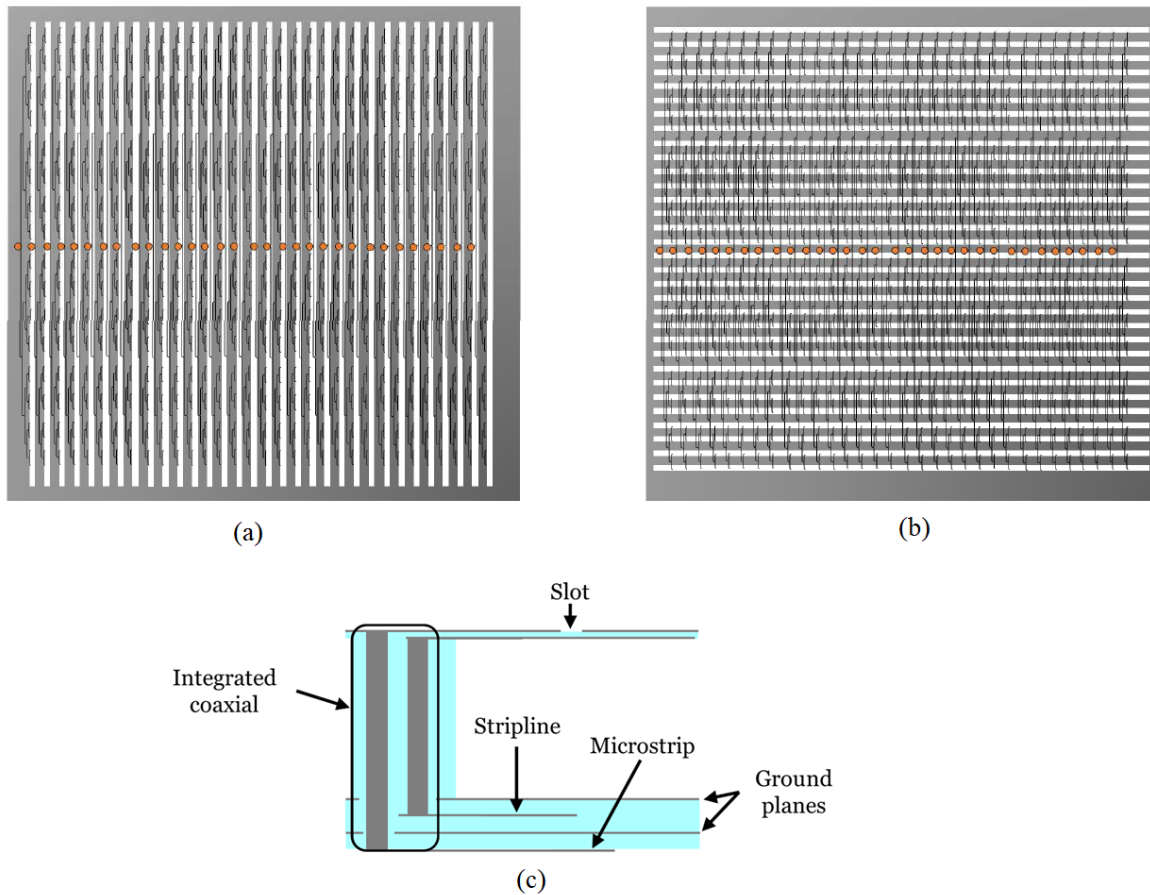


Figure 1.7: Corporate feeding network feeding in-phase all the elements on the same (a) slot, and (b) on the same column, but on different slots; (c) Array stack-up showing the array plane, the integrated coaxial, the stripline corporate feeding network, and the microstrip corporate feeding network.

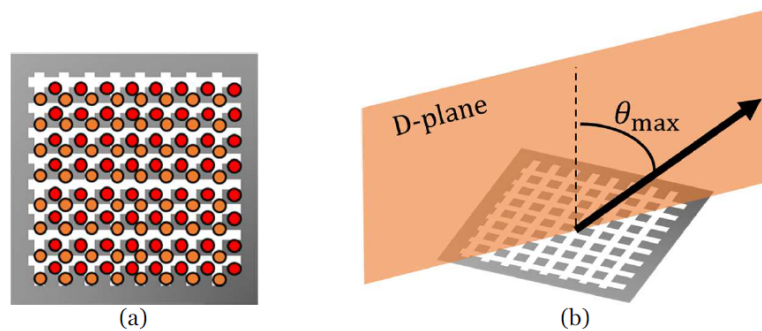


Figure 1.8: (a) Smaller array, with 8×8 elements, fully connectorized, to measure the cross-polarization of a central element for scanning in the diagonal plane (D-plane).

1.5. Outline of the Thesis

The main objective of this thesis is the design of the feeding structure for the array described in Sec. 1.4. This is based on integrated coaxial lines and microstrips or striplines. Moreover a novel feeding strategy is proposed to simplify the complexity and the costs of the unit cell. The new approach is based on replacing the coaxial lines with integrated parallel plate waveguides (PPW).

The thesis is organized as follows:

In **Chapter 2**, the feeding structure of the two orthogonal slots in each unit cell is designed, consisting of the integrated coaxial feed, and the coaxial to microstrip transition. For the case of the 8×8 array, the transition between the coaxial to sub-miniature push-on (SMP) connector is also designed.

In **Chapter 3**, the design of the corporate feeding network for the array is presented. This consists of two designs of 1-to-32 power dividers, one implemented with microstrip transmission lines and the other with striplines.

In **Chapter 4**, a novel PPW-based feeding structure is introduced to simplify the complexity of the integrated coaxial feed, and to reduce the total cost. Two examples of unit cell design, based on this new feed concept, are presented: one consists in a single-polarized array of connected slot, covering the band from 70 GHz to 140 GHz, for automotive radars; another example is referring to a dual-polarized connected slot array covering the same 2-8 GHz range, for wideband base stations.

Lastly, **Chapter 5** contains some concluding remarks on the thesis project. It also offers recommendations for future work.

The derivation of the impedances for 5-section Chebyshev transformers is shown in **Appendix A** and the final board prototype is shown in **Appendix B**.

2

Array with Integrated Coaxial Feed

2.1. Integrated Coaxial Introduction

In this section, an integrated coaxial transmission line is designed to feed the array. The concept of the integrated coaxial feeds is based on the traditional coaxial lines, which are sketched in Fig. 2.1(a). The well-known characteristic impedance expression of a coaxial transmission line is

$$Z_0 = \frac{60}{\sqrt{\epsilon_r}} \ln \frac{b}{a}, \quad (2.1)$$

where ϵ_r is the relative permittivity of the dielectric filling the coaxial, while b and a are the radii of the outer and inner conductor. In the integrated coaxial line, metallic pins distributed around the inner conductor replace the continuous outer conductor of the traditional coaxial, as shown in Fig. 2.1(b). Despite the outer conductor being made by pins is not closed, the distance between the pins can be chosen in such a way to minimize the field leakage outside the transmission line. In this method, the integrated coaxial can be implemented inside dielectric to transmit power between two layers in parallel. In some applications, the integrated coaxial needs to be connected with some transmission lines such

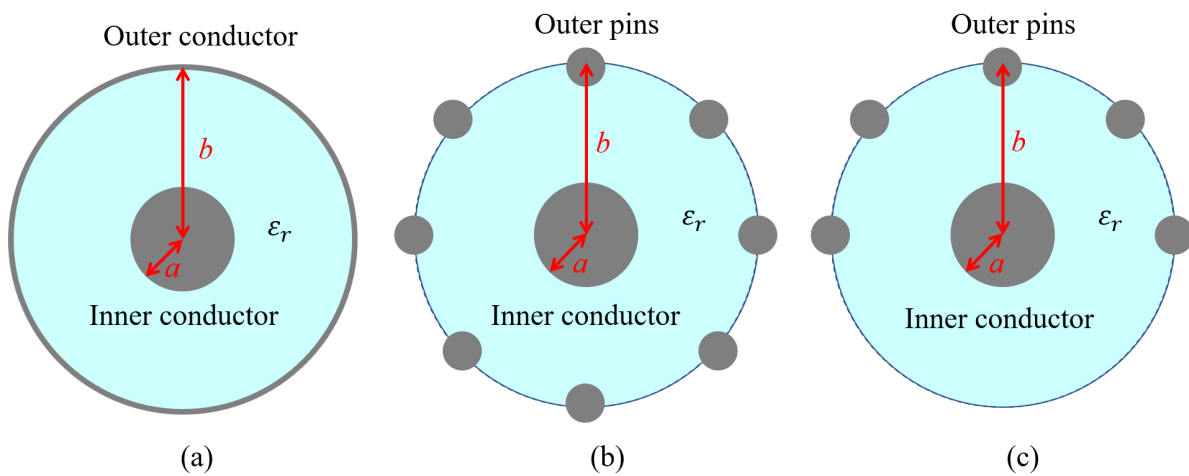


Figure 2.1: (a) Coaxial line; (b) Integrated coaxial line with pins all around the inner conductor; (c) Integrated coaxial line with pins around the inner conductor in semicircle.

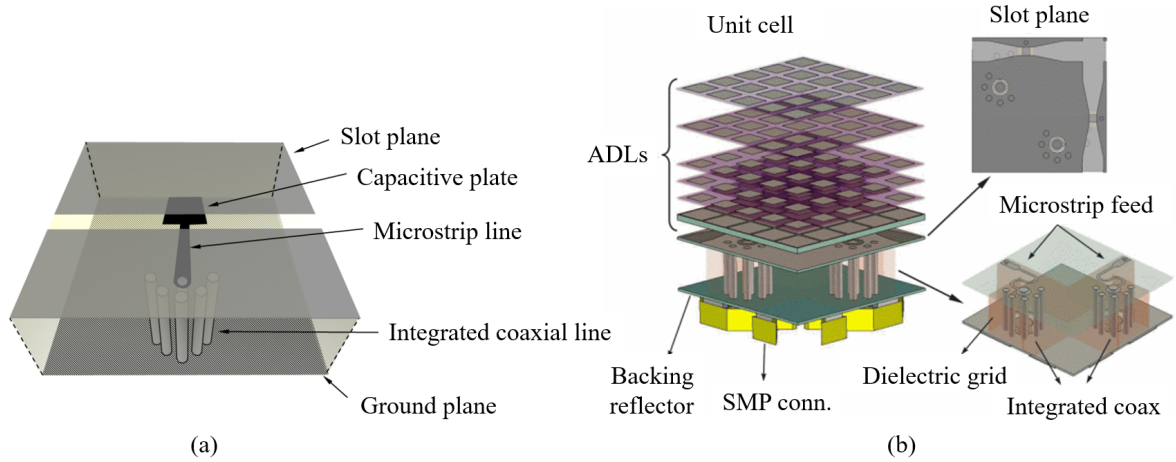


Figure 2.2: Sketch of integrated coaxial feed for arrays.

as microstrip, in which case, the outer pins are usually distributed in semicircle, and the positions of the pins are shown in Fig. 2.1(c). Two examples can be seen in Fig. 2.2(a) [39] and Fig. 2.2(b) [40].

The radius of the pins and distance between them as well as the number of the outer pins will influence the characteristic impedance of an integrated coaxial transmission line. In [41], Trainotti and Fano gave an analytical analysis of the characteristic impedance of an integrated coaxial where the outer pins distribute in a circle uniformly. However, the impedance expression for an integrated coaxial with outer pins in non-uniform positions, which is the case in this project, is not derived yet, so *CST STUDIO SUITE* is needed to run simulations to get the characteristic impedance desired.

2.2. Unit Cell

Before stepping into the detail of the integrated coaxial feed of this project, the two ADL superstrates for NB and WB as well as the connected array should be introduced.

The NB ADL superstrate is realized by four layers of patches, corresponding to a second order Chebyshev impedance transformer, while the WB ADL is realized using eight layers of patches, obtaining a fourth order Chebyshev impedance transformer. Moreover, a host medium has been introduced between the first two ADL layers both for the NB and WB, yielding an improved matching for scanning on the E-plane. In fact, the ADL in free space is transparent for the transverse magnetic (TM) incidence at large grazing angles, hence creating mismatch. However a host medium can be inserted between the first two layers of patches closest to the slots. Under this configuration, for the TM incidence, the effective permittivity of the ADL tends to the one of the host medium for grazing incidence, leading to smaller variation of the input impedance of the unit cell as a function of the scan angle in the E-plane. The 3-D models for the NB ADL superstrate and the WB ADL superstrate are shown in Fig. 2.3(a) and (b) respectively.

The ideal feed of the dual-pol connected array consists of a microstrip running across the slot, and printed on the opposite side of the thin dielectric where the slot array is printed on. The microstrip ends into a capacitive patch, as shown in Fig. 2.4(a), used to compensate the inductive effect of the ground plane. The slot is fed by a delta-gap generator with

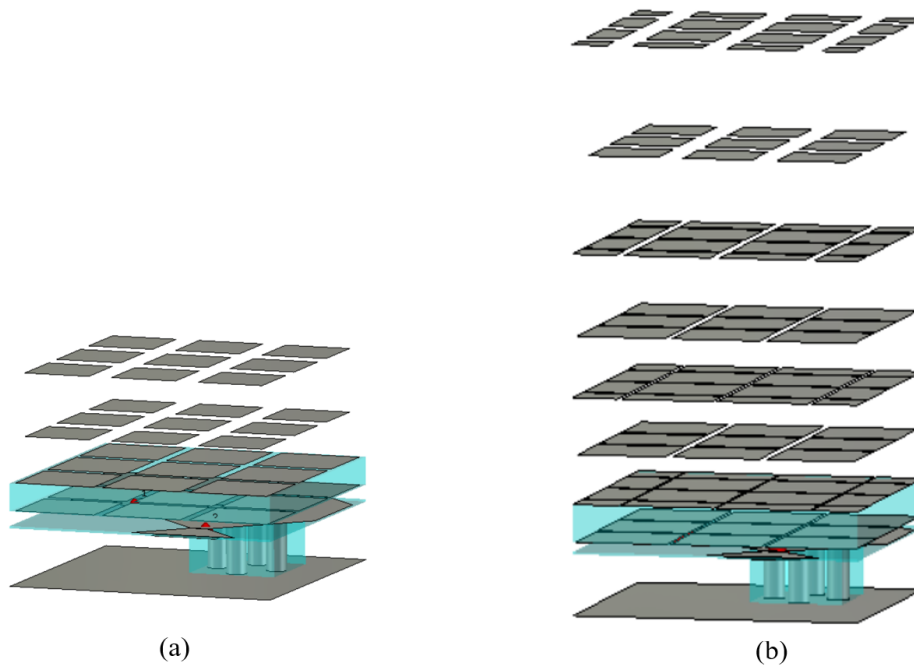


Figure 2.3: 3-D view of (a) NB ADL superstrate; (b) WB ADL superstrate above a slot.

impedance of 90Ω . The corresponding values of the active VSWR of this configuration for the NB and WB ADLs are shown in Fig. 2.4(b) and (c). For the NB ADL, the active VSWR < 2 for every scanning condition between 6 to 8 GHz. On the contrary for WB ADL, the active VSWR < 2.5 from 2.3 GHz to 8 GHz.

The ADL superstrates used in the unit cell design, up to this point, consisted only of the metal patches and the host medium (RT/Duroid 5880 $\epsilon_r=2.2$). However, additional materials have to be introduced such as foam layers (Rohacell foam, $\epsilon_r=1.06$) to sustain the structure, bonding layers (Arlon CuClad 6250, $\epsilon_r=2.35$) to bond together all the different materials, and thin dielectric films (DuPont Pyralux AP, $\epsilon_r=3.2$) to print the patches on (see Fig. 2.5(a)). The introduction of new materials in the ADL superstrates changes significantly the response, so the geometrical parameters of the layers have to be re-tuned to compensate such changes. This optimization process, which would be extremely time consuming with a commercial software due to the high complexity of the structure, can be done relatively simply thanks to the analytical formulation of the connected array and the ADL [30, 37, 42], which is valid for arbitrary layered media. Figure 2.5(b) and (c) show the active VSWR of the unit cell optimized after the introduction of the realistic materials in the stack-up.

This unit cell structure containing the two ADL superstrates and the connected array is designed by the PhD student Riccardo Ozzola, whose project is related to the work carried out in this thesis..

2.3. 32×32 Array with Integrated Coaxial Feed

2.3.1. Integrated Coaxial Feed

A more detailed feed design is presented including a transition to the connectors or to the feeding network placed below the ground plane. The feeding structure employed for the

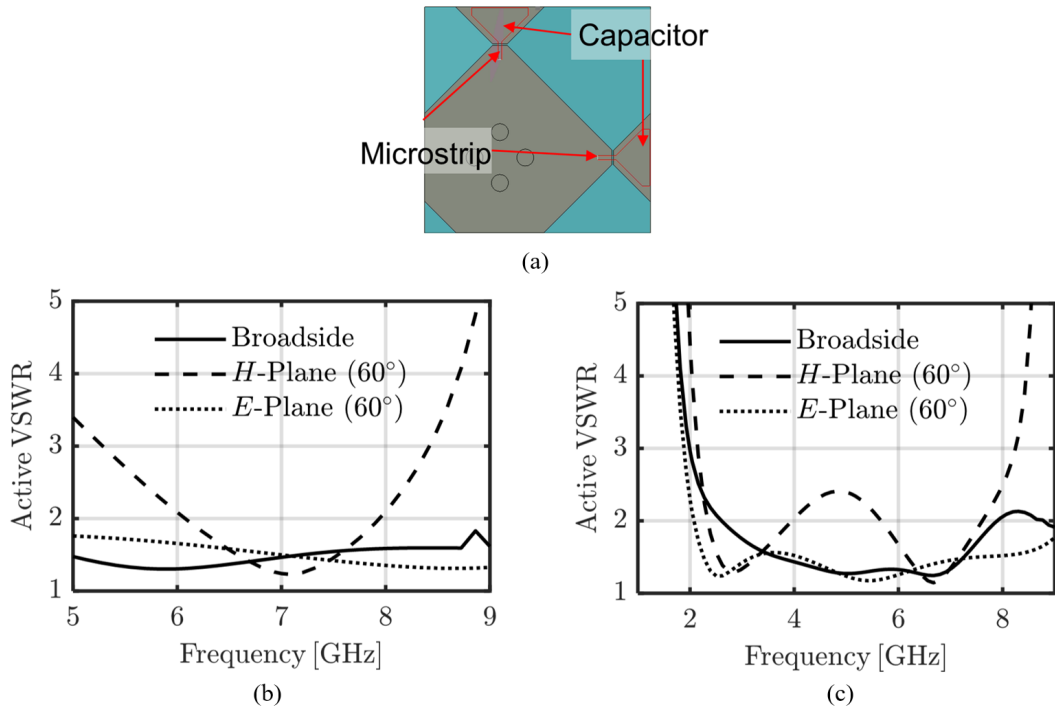


Figure 2.4: (a) Dual-pol unit cell excited with a microstrip ending into a capacitive patch and its corresponding active VSWR for the (b) NB and (c) WB ADL for broadside and scanning up to 60° in E- and H-planes.

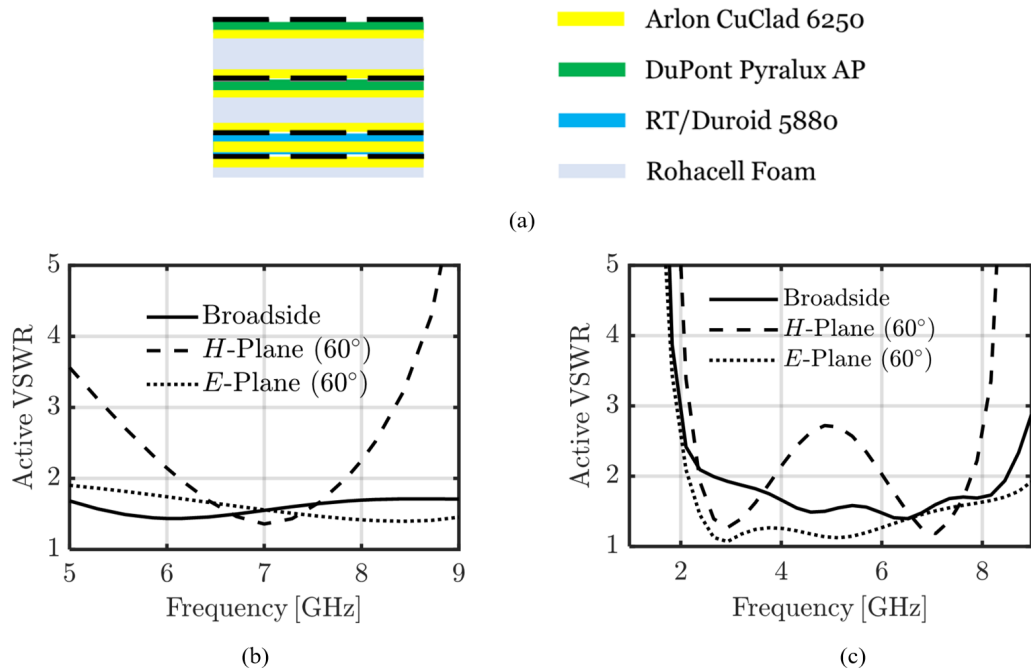


Figure 2.5: (a) Possible ADL stratification including the foam layers (Rohacell foam), the bonding layers (Arlon CuClad 6250), and the film layers (DuPont Pyralux AP), and active VSWR of the dual-pol unit cell with (b) NB, (c) WB ADL superstrate for broadside and for scanning up to $\pm 60^\circ$ on the main planes.

design is depicted in Fig. 2.6 and consists of the combination of a planar transmission line and an integrated coaxial line. The integrated coaxial line consists of seven vias: a central

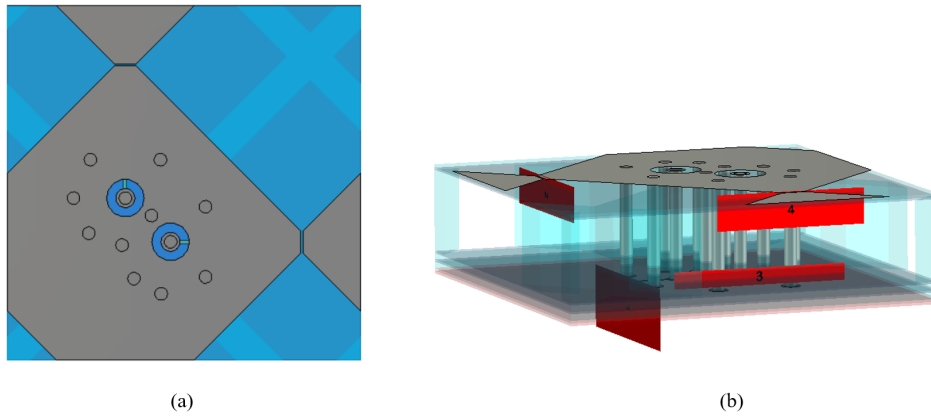


Figure 2.6: (a) Top view of the integrated feed; (b) 3-D view of the integrated feed.

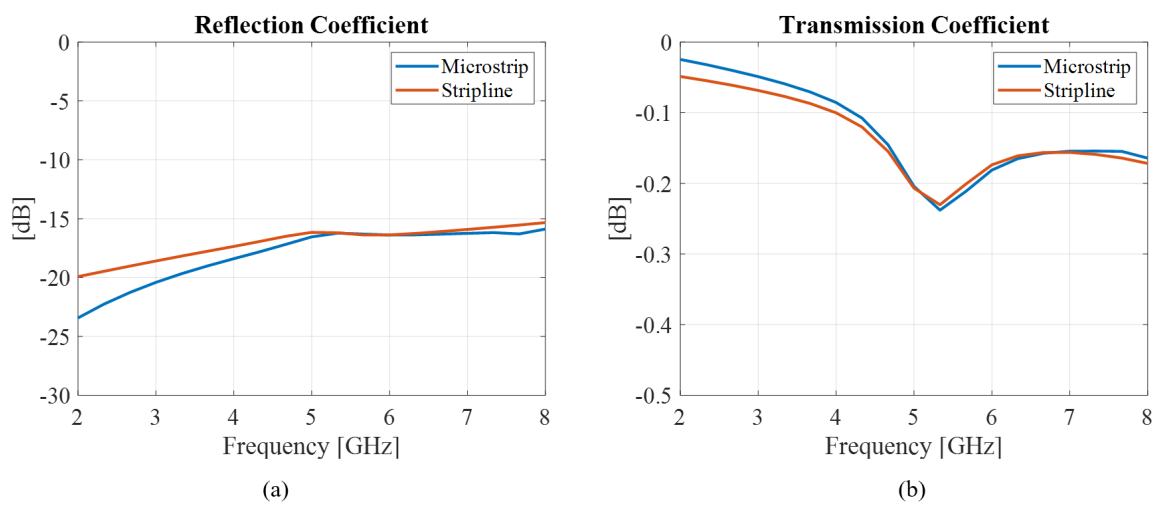


Figure 2.7: (a) Reflection coefficient of the integrated feed with microstrip and stripline; (b) Transmission coefficient of the integrated feed with microstrip and stripline.

via as the inner conductor and six vias that make up the outer conductor. A dielectric grid which is realized with a milled dielectric, is needed to sustain the structure and to allow the support for the vias, needed for the coaxial and also preventing parallel-plate-waveguide-like modes to propagate in the substrate. The coaxial line is connected at one end to the microstrip feeding the slot and, at the other end, to a microstrip that is below the ground plane (or to a stripline for the orthogonal slot). The performance of the microstrip-to-coax-to-microstrip transition and microstrip-to-coax-to-stripline transition is shown in Fig. 2.7. For both cases, the reflection coefficient for the entire transition is below -15 dB, as shown in Fig. 2.7(a), while the transmission coefficient is higher than -0.25 dB (Fig. 2.7(b)). The normalization impedances are 90Ω for the ports at the slot level, while 70Ω and 85Ω for the for the stripline and microstrip input ports, respectively.

2.3.2. Unit Cell with Integrated Coaxial Feed

The feeding structure is combined with the rest of the unit cell in Fig. 2.8(a) for the narrow-band design. The active reflection coefficient for this combination is shown in Fig. 2.8(b) for broadside scanning and in Fig. 2.8(c) for scanning to 60° in the main planes. It can

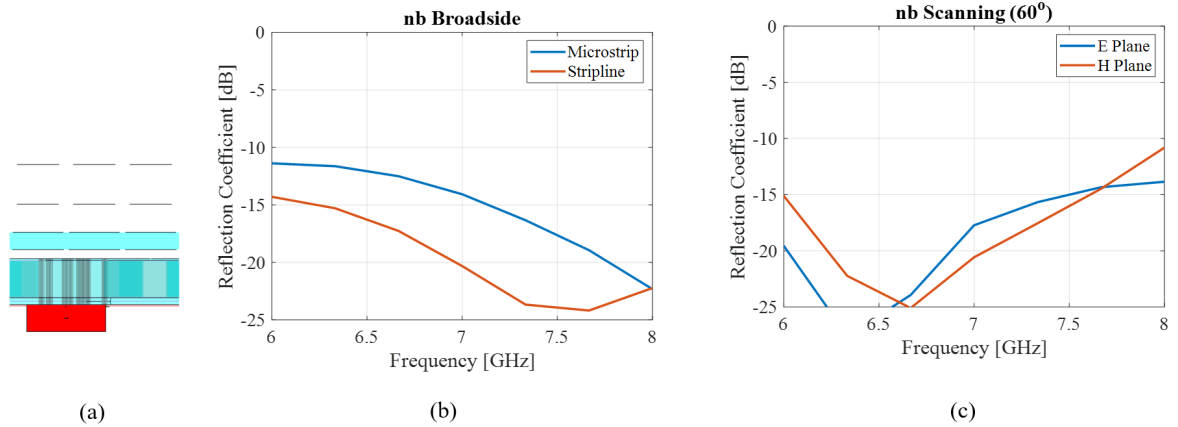


Figure 2.8: (a) Unit cell with NB ADL; Active reflection coefficient of the unit cell with NB superstates for (b) broadside, and (c) scanning up to 60° in E- and H-planes.

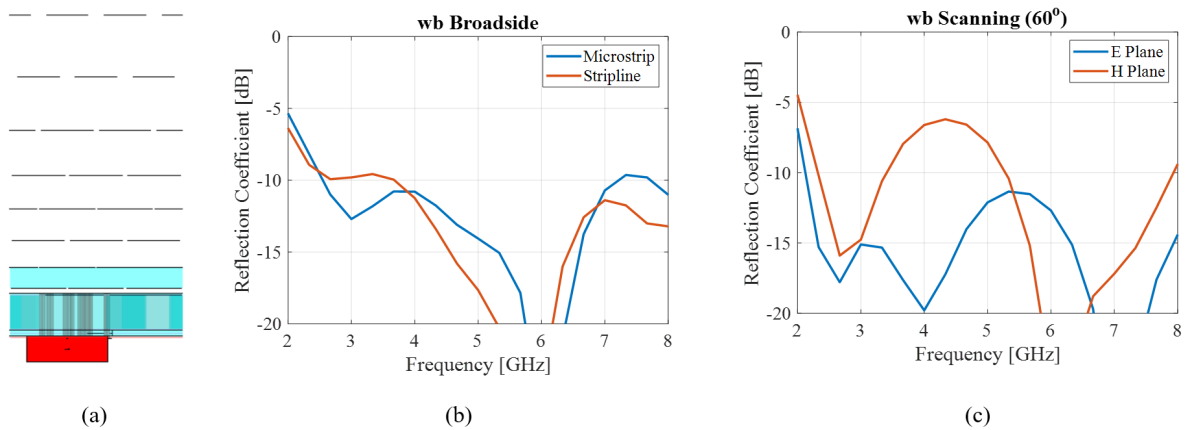


Figure 2.9: (a) Unit cell with WB ADL; Active reflection coefficient of the unit cell with WB superstates for (b) broadside, and (c) scanning up to 60° in E- and H-planes.

be seen that the active reflection coefficients are lower than -10 dB over the band of interest for both broadside and scanning up to 60° in E- and H-planes. Figure 2.9 shows the matching performance for wideband unit cell design. One can observe that for broadside, the active reflection coefficient is lower than -8 dB from 2.3 until 8 GHz, and a -6 dB bandwidth is achieved from 2.1 to 8 GHz for scanning up to 60° in E- and H-plane. The matching characteristics with this integrated feed are comparable to the one of the unit cell with the ideal feed.

2.4. 8×8 Array with Integrated Coaxial Feed

2.4.1. SMP Connector

Besides the large 32×32 array with corporate feeding networks combining sets of 32 elements, the plan is to realize a small version of the array with 8×8 elements for each polarization, where each element is connectorized. This will allow to measure the cross-polarization in arbitrary azimuthal planes. Moreover, the smaller array fully connectorized will allow also to measure the active reflection coefficient of a single element and to mea-

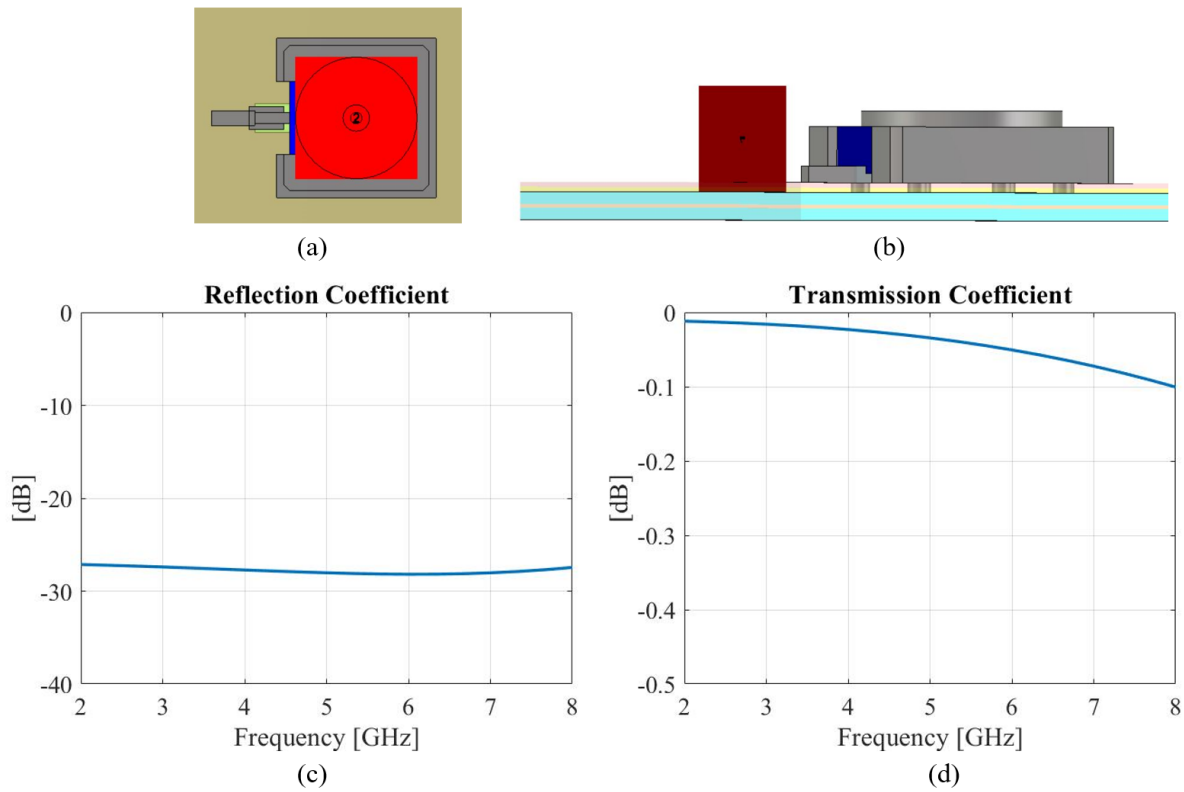


Figure 2.10: (a) SMP connector; (b) SMP connector with a 50 Ω microstrip line; (c) Reflection and (d) transmission coefficient of the model in (b).

sure radiation patterns of a relatively small array. For the small array design, the unit cell is connected directly with a SMP connector (19S141–40MS5), like the one shown in Fig. 2.10. A transition between the connector and a 50 Ω microstrip line has been optimized, and its performance in terms of reflection and transmission coefficients is presented in Fig. 2.10(c) and (d) respectively. It can be seen that the simulated reflection coefficient is lower than -26 dB and the transmission coefficient is larger than -0.1 dB.

The performance of the total transition, including the microstrip feeding the slot, the integrated coaxial line, the microstrip line below the ground plane and the SMP connector, is investigated in Fig. 2.11. The transition includes an impedance transformer to transfer the input impedance of the slot (90 Ω) to the lower impedance of the coaxial connector (50 Ω). The impedance transformer creates a typical resonance that can be observed in the reflection coefficient in Fig. 2.11(b). However, the level is below -13 dB, which corresponds to a transmission coefficient better than -0.21 dB as shown in 2.11(c).

2.4.2. Integrated Coaxial Feed with SMP Connectors and ADL

The feeding structure is combined with the rest of the unit cell in Fig. 2.12(a) for the narrow-band design. The active reflection coefficient for this combination for broadside scanning is shown in Fig. 2.12(b) and for scanning to 60° in the main planes in Fig. 2.12(c). It can be seen that the matching characteristics are comparable to the one of the unit cell for the large array. Figure 2.13 shows the model and matching performance for wideband unit cell design. Also this case achieves comparable result as the previous cases.

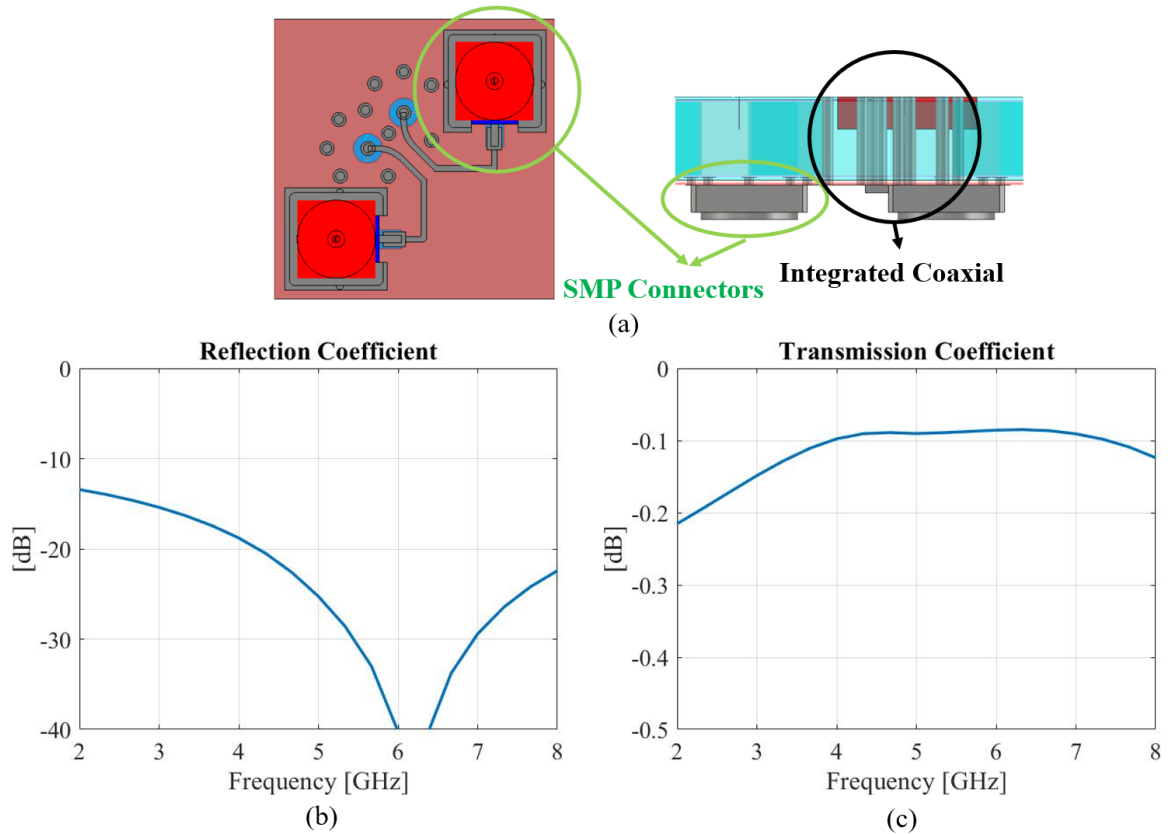


Figure 2.11: (a) Microstrip-to-SMP connector transition; (b) Reflection and (c) transmission coefficient of the model in (a).

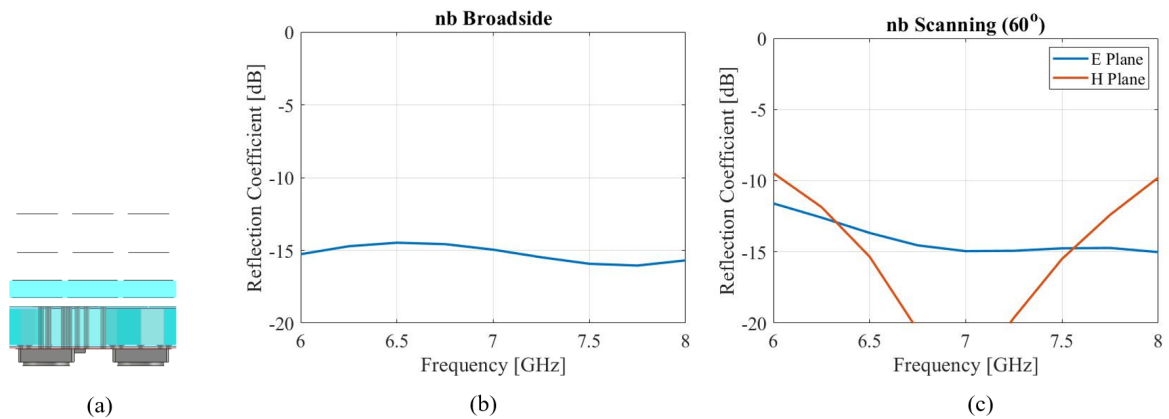


Figure 2.12: (a) Unit cell with SMP connectors and NB ADL; Active reflection coefficient for (b) broadside, and (c) scanning up to 60° in E- and H-planes.

2.5. Cross-Polarization Levels

A typical property of ADLs is that their effective refractive index is different for the TE and TM components of a plane-wave travelling through the artificial medium. This unequal behaviour can have the effect of increasing the cross-polarization (X-pol) levels when scanning off the main planes. Besides the ADLs, also the feeding structure with vertical vias and the mutual coupling between the two orthogonal slots can significantly influence the X-

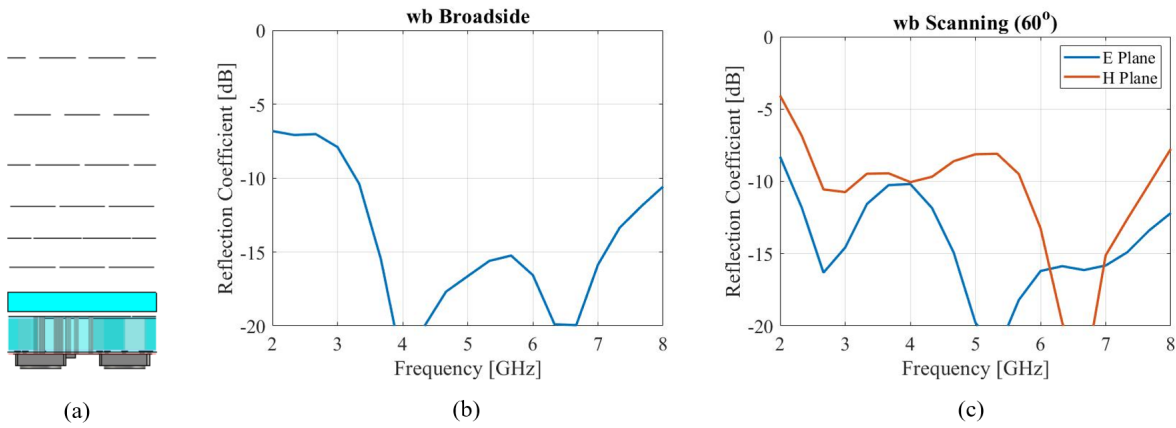


Figure 2.13: (a) Unit cell with SMP connectors and WB ADL; Active reflection coefficient for (b) broadside, and (c) scanning up to 60° in E- and H-planes.

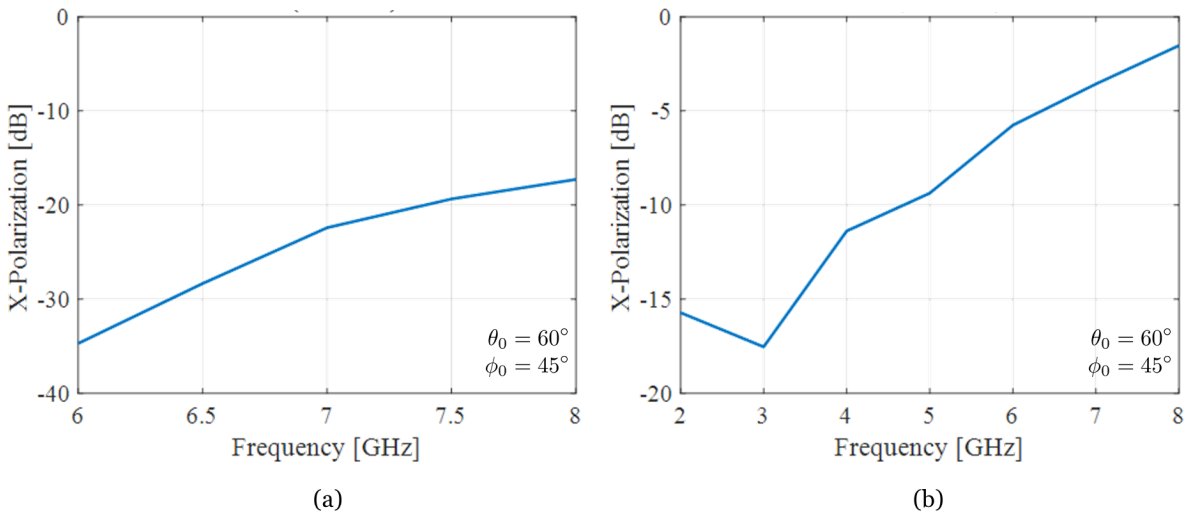


Figure 2.14: Cross-Polarization levels of the dual-pol unit cell with the integrated coaxial feed for (a) NB and (b) WB ADL, while scanning to $\theta = 60^\circ$ in the D-plane ($\phi = 45^\circ$).

pol levels of the unit cell. Figure 2.14 shows the X-pol level for the NB and WB unit cells as a function of the frequency, and for scanning to 60° in the diagonal plane. It is evident that the X-pol level remains below -18 dB for the NB array as shown in Fig. 2.14(a). The obtained value is lower than the typical -10 dB, pertinent to the Wheeler’s current in free space under the same scanning conditions. Thus, in the NB case the combination of the ADL and the feeding structure seems to be beneficial and reduce the X-pol that the array would have without ADLs.

On the other hand, the WB unit cell exhibits higher X-pol level, as shown in Fig. 2.14(b). The X-pol is low for the low end of the frequency band, but increases with frequency, which is typical of the connected array with ADL loading. The highest value is around -2 dB for the highest frequency of operation (8 GHz). Although such a value is high, it was shown in [43] that the two orthogonal slots can be combined with a proper set of weights so that the X-pol can be cancelled over a wide frequency and angular range. This allows to realize arbitrary slant linear polarization with excellent polarization purity.

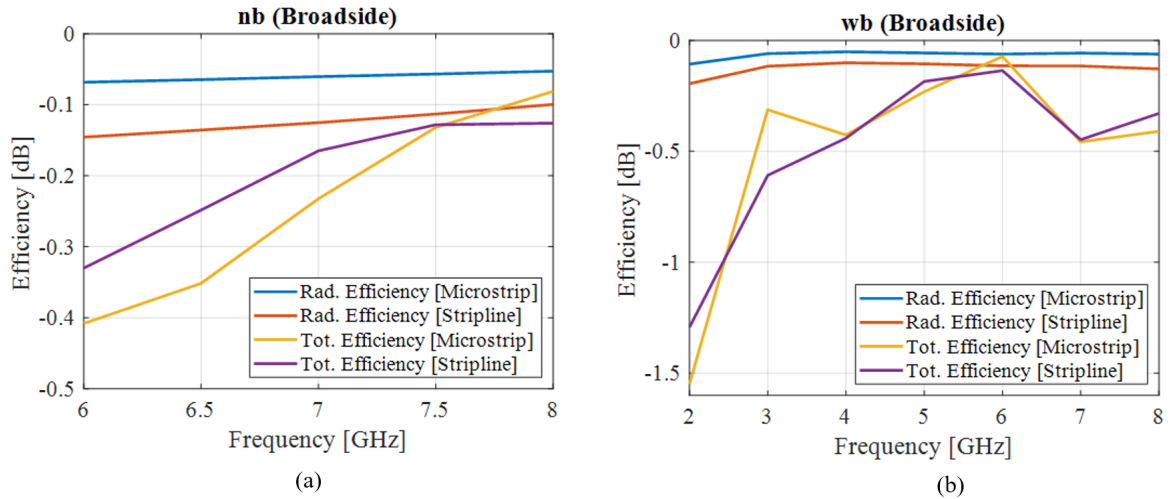


Figure 2.15: Total and radiation efficiency of the dual-pol unit cell with the integrated coaxial feed for (a) NB and (b) WB ADL, while scanning to broadside.

2.6. Simulated Unit Cell Efficiency

The total efficiency of the unit cell was also simulated in *CST DESIGN ENVIRONMENT*, accounting for the material losses. The metal is assumed to be copper, with a conductivity of 5.8×10^7 , while the dielectric materials include the dissipation factor ($\tan\delta$) as specified in the datasheet. The resulting efficiency is shown in Fig. 2.15, for the NB and the WB cases, respectively. The radiation efficiency (due to Ohmic and dielectric losses) is higher than -0.2 dB for the WB design and -0.15 dB for the NB design. These values correspond to efficiencies larger than 95%, confirming the low loss properties of artificial dielectrics.

The total efficiency, including mismatch losses, is also shown and is better than -0.4 dB for the NB case, and better than -0.6 dB for most of the band in the WB case, degrading to -1.6 dB at 2 GHz in accordance with the increased mismatch of the unit cell at the lowest frequency (see Fig. 2.9).

3

Design of Wideband Corporate Feeding Network

The array prototype is to be manufactured with separate connectors for each column of the array, while the rows of elements are combined by means of corporate feeding networks. This is realized with 1-to-32 power combiners that feed with equal amplitudes and phases a row of connected slot elements for one polarization and a row of parallel slots for the other polarization. On the contrary, in the orthogonal plane with respect to the corporate networks, the inputs are left separate with individual connectors, so that different scanning conditions can be realized by post-processing of the embedded patterns.

The critical aspects of the corporate feeding network design are the large bandwidth, which spans over two octaves, from 2 to 8 GHz, and the limited area available for the design, since the entire 1-to-32 combiner must fit within the unit cell period of 15 mm. Actually the usable area is even smaller than the unit cell, since the lines cannot overlap with the many vias present in the unit cell to compose the vertical coaxial lines. The feeding networks will be embedded in the same PCB stack that will be used to realize the connected array itself, below the backing reflectors.

3.1. Theoretical Background

3.1.1. T-junctions

The required 1-to-32 corporate feeding network is actually a cascade of T-junctions, progressively combining 2^n elements, with $n \in [1, 2, 3, 4, 5]$. Figure 3.1 shows a T-junction [44]

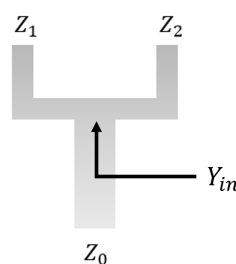


Figure 3.1: Microstrip based T-junction.

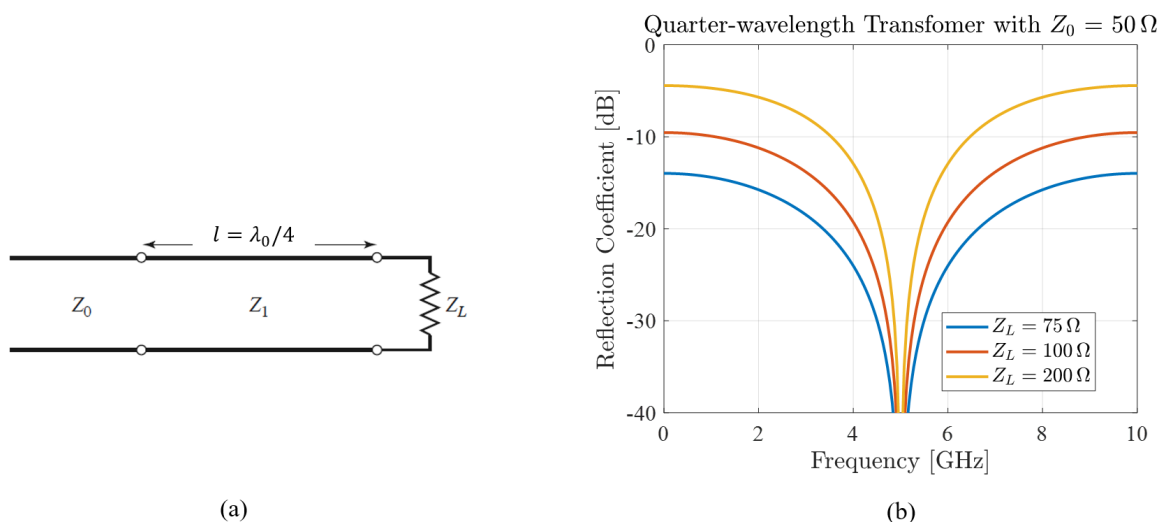


Figure 3.2: (a) Quarter-wavelength transformer, where λ_0 is the wavelength of center frequency; (b) Reflection coefficients of quarter-wavelength transformers with transformation ratios $Z_L/Z_0 = 1.5, 2$ and 4 .

with output impedances Z_1 and Z_2 . In order for the T-junction to be matched to an input transmission line with characteristic impedance Z_0 , the input admittance should verify the condition

$$Y_{in} = \frac{1}{Z_1} + \frac{1}{Z_2} = \frac{1}{Z_0}. \quad (3.1)$$

If $Z_1 = Z_2$, then

$$Z_0 = \frac{Z_1}{2} = \frac{Z_2}{2}. \quad (3.2)$$

As the characteristic impedance of the combined output is lower than that of the two input lines, if for example the T-junction is realized with microstrip lines, the width of the transmission line will become wider. Thus, when cascading multiple T-junctions, the impedance will become lower and lower, resulting in wider and wider transmission lines. Since the space occupation is a constraint in this design, to avoid microstrip lines with very low impedance and large width, impedance transformers need to be implemented to raise the impedance and decrease the width of lines. However, while the condition (3.2) is frequency independent and ensures very large bandwidth, the introduction of impedance transformers gives rise to a frequency dependence that limits the bandwidth. For this reason, wideband multi-section transformers will be employed in the design, targeting the large bandwidth of operation 2-8 GHz.

3.1.2. Impedance Transformers

- *Quarter-Wavelength Transformer*

The quarter-wavelength transformer is the simplest impedance transformer, which is shown in Fig. 3.2(a). In order to match a load Z_L with transmission line Z_0 , the length of the transformer needs to be $l = \lambda_0/4$, where λ_0 is the wavelength of the transmission line section at the center frequency f_0 . The characteristic impedance of the transformer is given by $Z_1 = \sqrt{Z_0 Z_L}$.

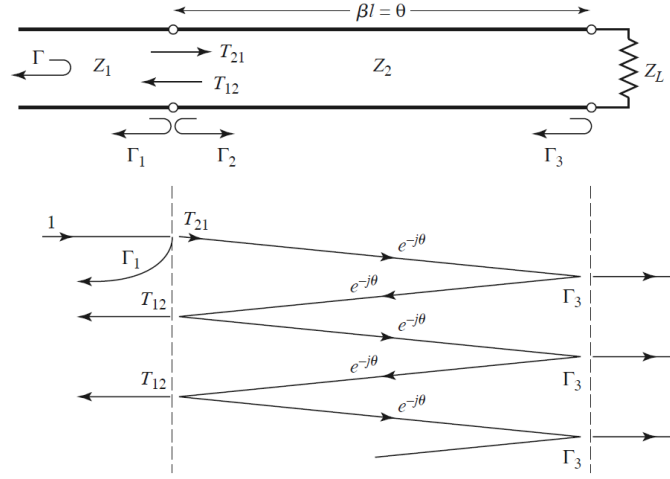


Figure 3.3: Partial reflections and transmissions on a single-section matching transformer. [44]

The reflection coefficient of quarter-wavelength transformers with center frequency 5 GHz is shown in Fig. 3.2(b), for different transformation ratios. It can be seen that with smaller Z_L/Z_0 , the matching performance of the transformer improves, both in terms of bandwidth and reflection coefficient levels. However, when the transformation ratio is too large, a single quarter-wavelength transformer cannot achieve a sufficiently low reflection coefficient within a wide band. In this case, multi-section transformers can be used to meet the design requirements.

- *Small Reflection Model*

In the current design of the feeding network, multi-section transformers are implemented to raise the transmission line impedance to sufficiently high desired level, which yields a thin enough microstrip line that fits the available area. Before stepping into the design of multi-section transformers, a method to calculate approximately the total reflection coefficient due to the partial reflections from several small mismatch of impedance shall be introduced, which is called the theory of small reflections [45].

For a single-section transformer as shown in Fig. 3.3(a), the total reflection can be expressed as an infinite sum of partial reflections and transmissions as follows:

$$\begin{aligned}
 \Gamma &= \Gamma_1 + T_{12} T_{21} \Gamma_3 e^{-2j\theta} + T_{12} T_{21} \Gamma_3^2 \Gamma_2 e^{-4j\theta} + \dots \\
 &= \Gamma_1 + T_{12} T_{21} \Gamma_3 e^{-2j\theta} \sum_{n=0}^{\infty} \Gamma_2^n \Gamma_3^n e^{-2nj\theta} \\
 &= \Gamma_1 + \frac{T_{12} T_{21} \Gamma_3 e^{-2j\theta}}{1 - \Gamma_2 \Gamma_3 e^{-2j\theta}}. \tag{3.3}
 \end{aligned}$$

With partial reflection and transmission coefficients $\Gamma_2 = -\Gamma_1$, $T_{21} = 1 + \Gamma_1$, $T_{12} = 1 - \Gamma_1$, the total reflection coefficient can then be expressed as

$$\Gamma = \frac{\Gamma_1 + \Gamma_3 e^{-2j\theta}}{1 + \Gamma_1 \Gamma_3 e^{-2j\theta}}. \tag{3.4}$$

Assuming each reflection is small so that $|\Gamma_1\Gamma_3 = 1|$, then it can be approximately derived that the total reflection coefficient is

$$\Gamma \approx \Gamma_1 + \Gamma_3 e^{-2j\theta}. \quad (3.5)$$

From this equation, it can be seen that the total reflection is dominated by the initial reflection (Γ_1 between Z_1 and Z_2) and the last reflection (Γ_3 between Z_2 and Z_L). The term $e^{-2j\theta}$ represents the phase delay. Similarly, the total reflection for multiple sections can be derived as

$$\Gamma(\theta) = 2e^{-2jN\theta} \left[\Gamma_0 \cos N\theta + \Gamma_1 \cos(N-2)\theta + \dots + \Gamma_n \cos(N-2n)\theta + \dots + \frac{1}{2}\Gamma_{N/2} \right] \quad (3.6)$$

when N is even, or

$$\Gamma(\theta) = 2e^{-2jN\theta} \left[\Gamma_0 \cos N\theta + \Gamma_1 \cos(N-2)\theta + \dots + \Gamma_n \cos(N-2n)\theta + \dots + \Gamma_{(N-1)/2} \cos \theta \right] \quad (3.7)$$

when N is odd.

These formulas imply that by properly choosing the reflection coefficient of each section Γ_n and the number of sections N , any desired total reflection coefficient can be synthesized and derived. In the following, two multi-section common types of impedance transformers will be introduced and described using this theory.

- *Binomial Multi-Section Transformer*

A binomial multi-section transformer is characterized by a maximally flat response centered at the design frequency. By imposing the first $N-1$ derivatives of $|\Gamma(\theta)|$ to be equal to 0 at the center frequency, the total reflection coefficient magnitude can be expressed in the form

$$|\Gamma(\theta)| = |A(1 + e^{-2jN\theta})^N| = |A| |e^{-j\theta}|^N |e^{j\theta} + e^{-j\theta}|^N = 2^N |A| |\cos \theta|^N \quad (3.8)$$

where the constant A can be determined by recognizing that, for the low frequency limit $f \rightarrow 0$,

$$\Gamma(0) = 2^N A = \frac{Z_L - Z_0}{Z_L + Z_0} \quad (3.9)$$

from which

$$A = 2^{-N} \frac{Z_L - Z_0}{Z_L + Z_0}. \quad (3.10)$$

Then expand $\Gamma(\theta)$ according to the binomial expansion

$$|\Gamma(\theta)| = |A| \left| \sum_{n=0}^N C_n^N e^{-2jn\theta} \right| \quad (3.11)$$

where the binomial coefficients are $C_n^N = N! / [(N-n)!n!]$.

For each section of the N -section binomial transformer, the length is a quarter wavelength and the characteristic impedance of the $(n+1)^{th}$ section can be calculated by

$$\ln \frac{Z_{n+1}}{Z_n} \approx 2(2^{-N}) \frac{Z_L - Z_0}{Z_L + Z_0} C_n^N. \quad (3.12)$$

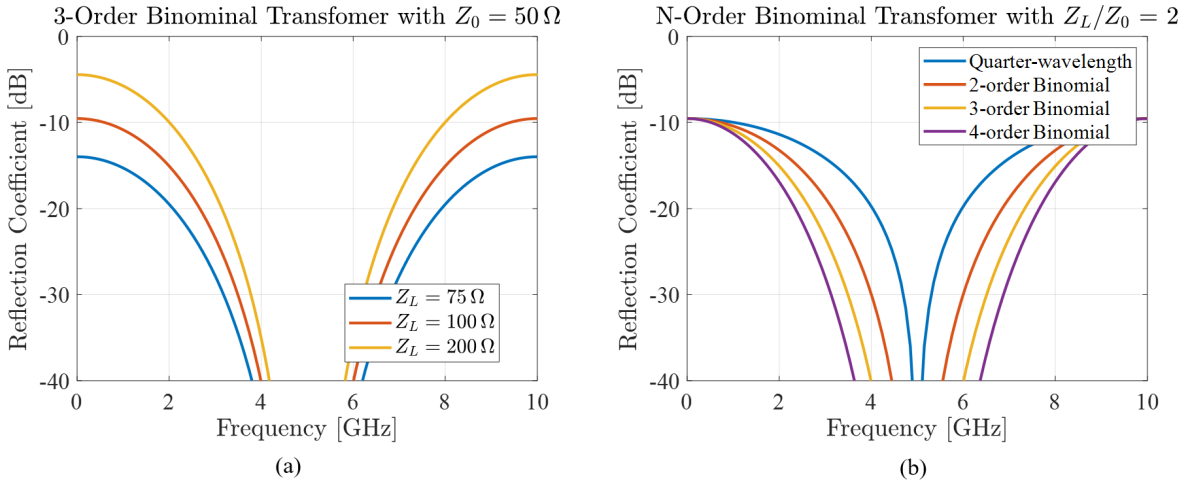


Figure 3.4: Reflection coefficient of binomial transformers with (a) three sections and different $Z_L/Z_0 = 1.5, 2, 4$ and (b) with different number of sections $N = 2, 3, 4$. A comparison between a single quarter-wave section and binomial transformers is shown as well.

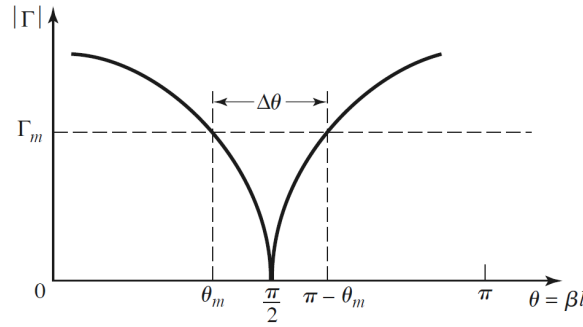


Figure 3.5: Approximate behaviour of the reflection coefficient magnitude defining a pass-band $\Gamma < \Gamma_m$ as a function of the phase $\theta = \beta l$, where β and l are the phase constant and the length of the transformer line, respectively. [44]

For example, the reflection coefficients of a three-order binomial transformer with center frequency 5 GHz is shown in Fig. 3.4(a), for different transformation ratios. It can be obtained that with smaller Z_L/Z_0 , the bandwidth of the binomial transformer increases and the reflection levels are lower for frequencies different from the design frequency. For fixed Z_L/Z_0 , the binomial transformers have larger bandwidth, proportionally to the number of sections N used.

- *Chebyshev Multi-Section Transformer*

In contrast with the binomial transformer, the multi-section Chebyshev transformer optimizes the bandwidth at the expense of the passband ripple. By equating $\Gamma(\theta)$ to a Chebyshev polynomial, the expression of total reflection coefficient will be

$$\Gamma(\theta) = Ae^{-jN\theta} T_N(\sec\theta_m \cos\theta), \quad (3.13)$$

where N is the number of sections and $T_N(\sec\theta_m \cos\theta)$ is Chebyshev polynomial of order N and θ_m is the lower edge of the passband $\Gamma < \Gamma_m$, as shown in Fig. 3.5.

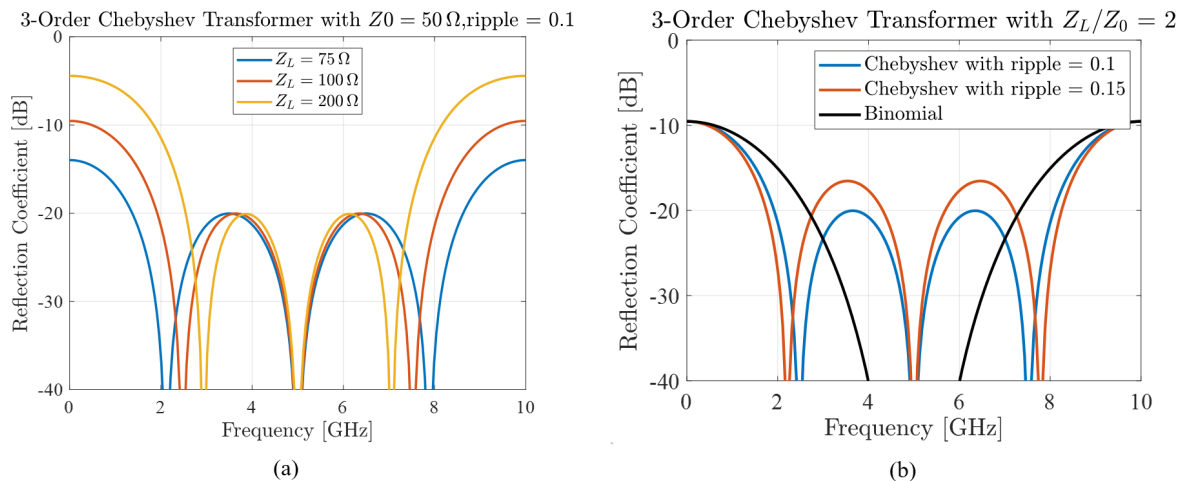


Figure 3.6: 3-order Chebyshev transformers with different (a) $Z_L/Z_0 = 1.5, 2, 4$ and (b) ripples = 0.1, 0.15. A compare between 3-order Chebyshev and 3-order Binomial transformer is shown as well.

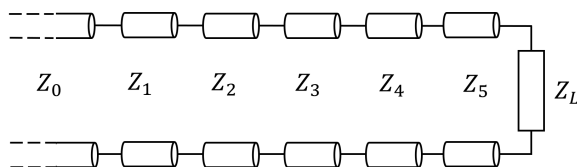


Figure 3.7: Model of a 5-section Chebyshev transformer.

For a three-order Chebyshev transformer with ripple of 0.1 (corresponding to -20 dB), the reflection coefficient with center frequency 5 GHz is shown in Fig. 3.6(a). For a higher-ripple Chebyshev transformer, a larger bandwidth can be achieved, as shown in Fig. 3.6(b). There is a trade-off between the ripple level and the bandwidth. By comparing the performance of binomial transformer and Chebyshev transformer in Fig. 3.6(b), it can be observed that the Chebyshev transformer has steeper slope and larger bandwidth than the binomial transformer, but higher reflection levels within the bandwidth due to the ripples.

In [44], the design parameters for Chebyshev transformers up to 4 sections are shown. However, a 5-section Chebyshev transformer as in Fig. 3.7 will be used in the design presented here. For this reason, the derivation of the characteristic impedance Z_1, Z_2, \dots, Z_5 for a five-order Chebyshev transformer is described in Appendix A.

3.2. Corporate Feeding Network

In this section, two corporate feeding networks with microstrips and striplines are designed. The corporate feeding network should meet the requirements below:

1. It should fit into the unit cell, while avoiding the overlap with the metal vias of the integrated coaxial lines.
2. It should divide the power from one input port to 32 output ports.
3. The reflection coefficient should be at least lower than -10 dB over the band 2-8 GHz.
4. The 32 output ports should have ideally equal amplitudes and phases. In practice the

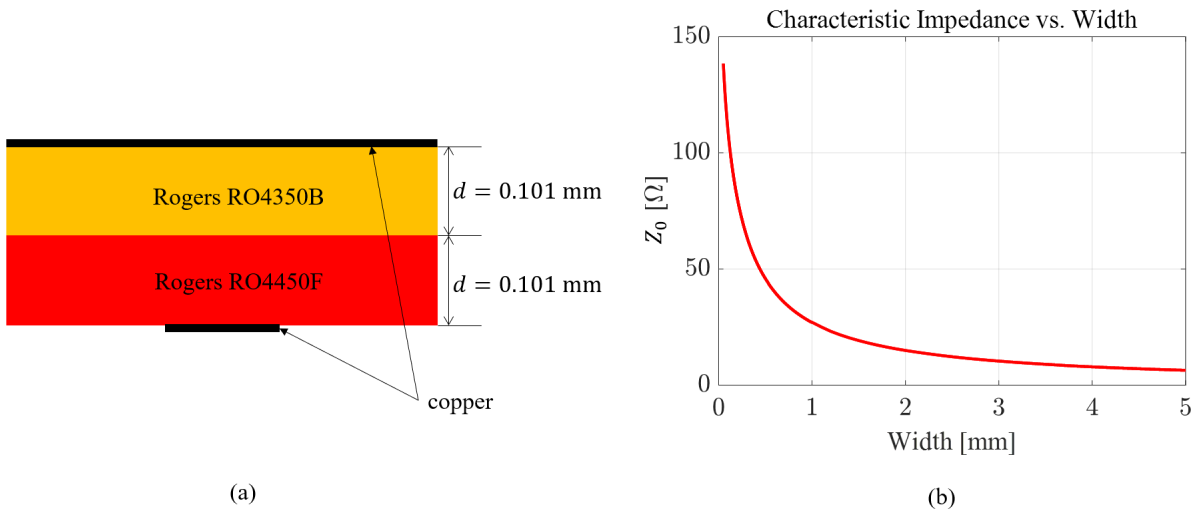


Figure 3.8: (a) Stack-up of the microstrip corporate feeding network; (b) Impedance versus width of microstrip.

Material	Type	Thickness [μm]	ϵ_r
Rogers RO4350B	Dielectric	101	3.66
Rogers RO4450F	Bonding Layer	101	3.52

Table 3.1: Properties of the dielectric for microstrip.

target performance is an amplitude variation across the output elements lower than 2 dB and phase variation lower than 10° .

3.2.1. Microstrip Feeding Network

The properties of dielectric on which the microstrip is printed is listed in Table. 3.1 and the sketch is shown in Fig. 3.8(a). In order to optimize the design, a lookup table of the characteristic impedance versus the microstrip width has been realized by simulations in *ANSYS Electronics Desktop*, taking into account also the copper thickness ($18 \mu\text{m}$), as shown in Fig. 3.8(b).

The 1-to-32 feeding network has to fit into $480 \text{ mm} \times 15 \text{ mm}$ narrow area and operates from 2 to 8 GHz with a good reflection coefficient. The design of the 1-to-32 microstrip feeding network starts with a T-junction, or a 1-to-2 power divider, as shown in Fig. 3.9(a). The T-junction assumes 90Ω as the load impedance of the two output ports, while the input port is 45Ω , according to the frequency independent condition in (3.2). No impedance transformation is included at this level, because of the electrical short length of the line. The 1-to-4 divider is shown in Fig. 3.9(b). In order to avoid too wide microstrip lines, a single quarter-wavelength transformer is implemented in the two arms. Then, in the next two cascades in Fig. 3.9(c) and (d), a 3-order and a 5-order Chebyshev transformers are implemented, respectively. The ripples of the Chebyshev response are kept low enough to guarantee good matching within the large operative band. For the final cascade, a long taper transformer is used to increase the input impedance up to 100Ω for the two halves of the network, so that at the input port of the feeding network an impedance of 50Ω will be

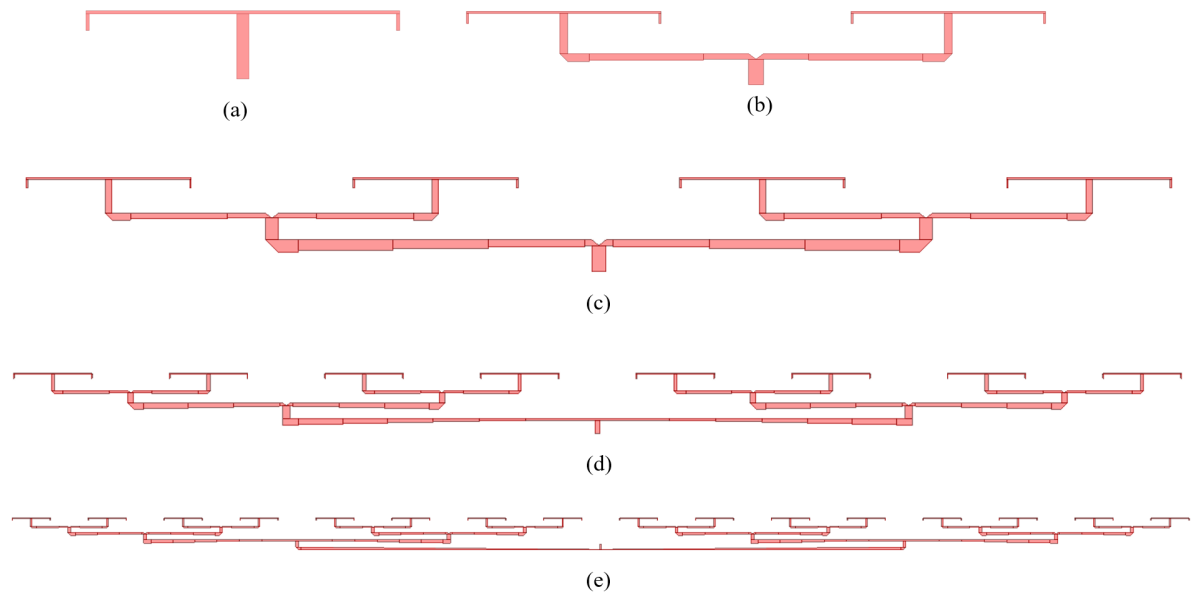


Figure 3.9: (a) 1-to-2; (b) 1-to-4; (c) 1-to-8; (d) 1-to-16; (e) 1-to-32 microstrip power divider.

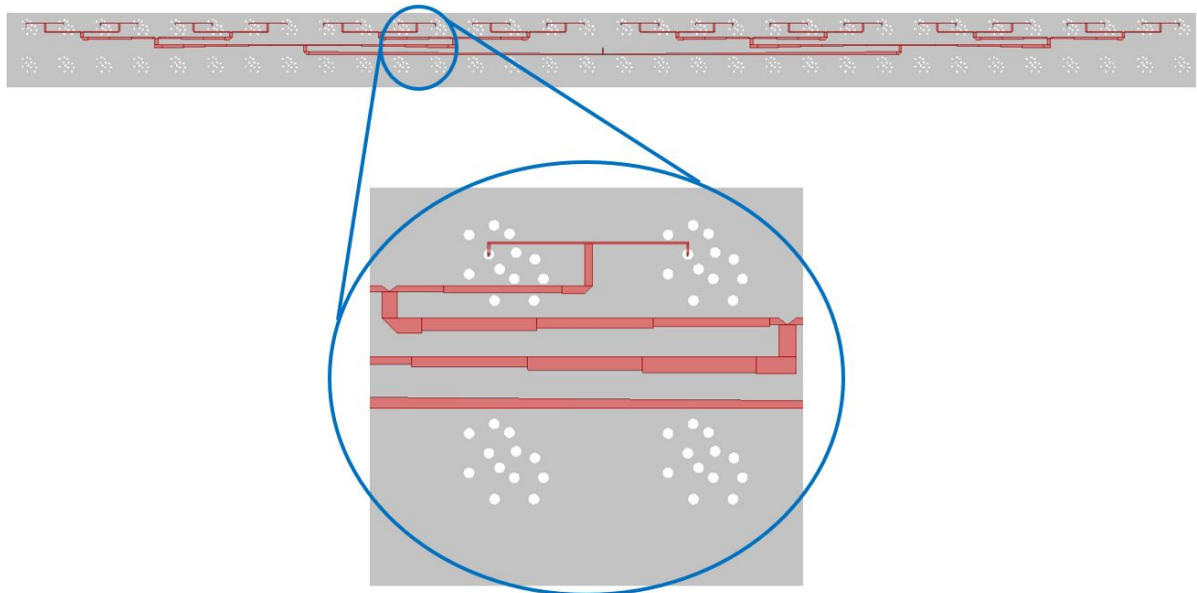


Figure 3.10: Microstrip corporate feeding network with metal vias allocated.

seen, which is easy for later connection with connectors. The final 1-to-32 power divider is shown in Fig. 3.9(e) and port 1 is the input port, while port 2,3,...,33 are the output ports.

It can be also observed from Fig. 3.10 that the space to allocate the divider is limited, thus the network is characterized by a narrow form factor, that can create some cross-talk between parallel lines that are close to each other. Moreover, some of the lines run between the vias of the integrated coaxial feeds to use more efficiently the available space.

The simulated S-parameters for the 1-to-32 power divider are shown in Fig. 3.11(a). It can be observed that the S_{11} is below -14 dB over the entire bandwidth, while the S_{1n} parameter ($n=2,\dots,33$) are below but close to the ideal value of -15 dB. The difference is due to losses, as it can be seen from Fig. 3.11(b), which shows 0.5 to 1.6 dB of Ohmic losses.

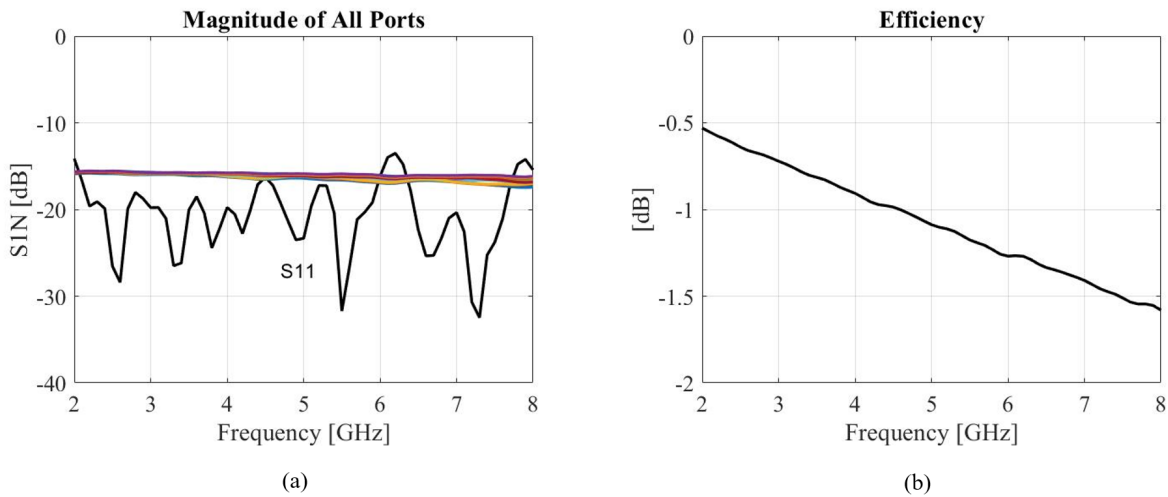


Figure 3.11: Simulated (a) S-parameters and (b) total efficiency of the 1-to-32 microstrip power divider.

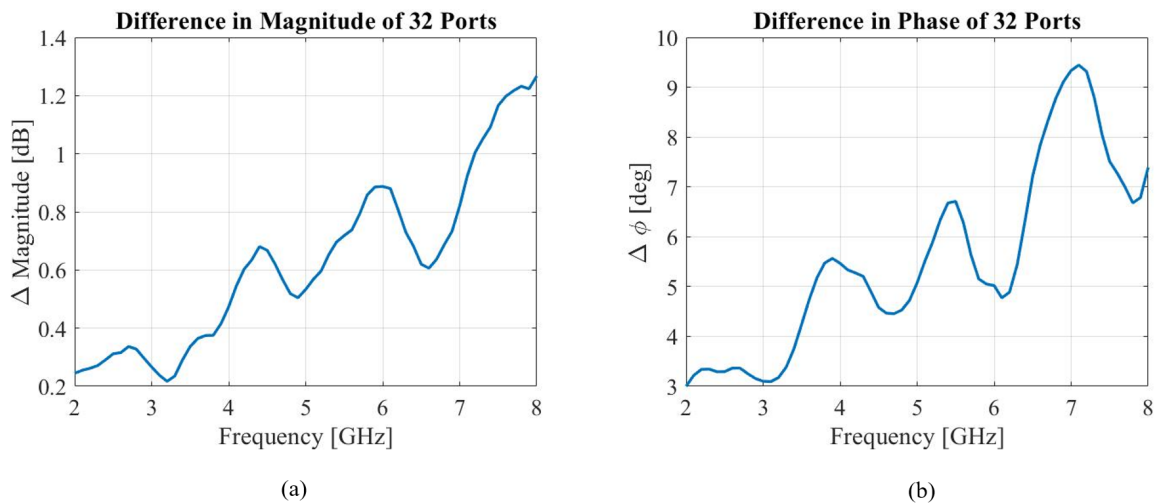


Figure 3.12: (a) Amplitude and (b) phase variation of the output ports for the 1-to-32 microstrip power divider.

The simulation includes dielectric losses in the substrate, as well as finite conductivity of the lines (copper) and surface roughness as specified by the material data sheet.

Ideally the S_{1n} curves should be all equal in amplitude and phase, but variation occurs due to the non-uniform cross coupling between the lines within the feeding network. The amplitude and phase variation of the different outputs are shown in Fig. 3.12. The amplitude variation increases with frequency, reaching about 1.2 dB at 8 GHz. The phase variation is also worse at the high end of the frequency band, but remains below 10° .

3.2.2. Stripline Feeding Network

Following the same design procedure, the dielectric stratification for stripline is listed in Table. 3.2 and the sketch is shown in Fig. 3.13(a). A lookup table of the characteristic impedance versus the stripline width is shown in Fig. 3.13(b).

The designed 1-to-32 stripline power divider is shown in Fig. 3.14, which is similar to the microstrip design. The simulated performance of the divider is shown in Fig. 3.15 and

Material	Type	Thickness [μm]	ϵ_r
Rogers RO5880	Dielectric	254	2.2
Arlon Cuclad 6700	Bonding Layer	76	2.35

Table 3.2: Properties of the dielectric for stripline.

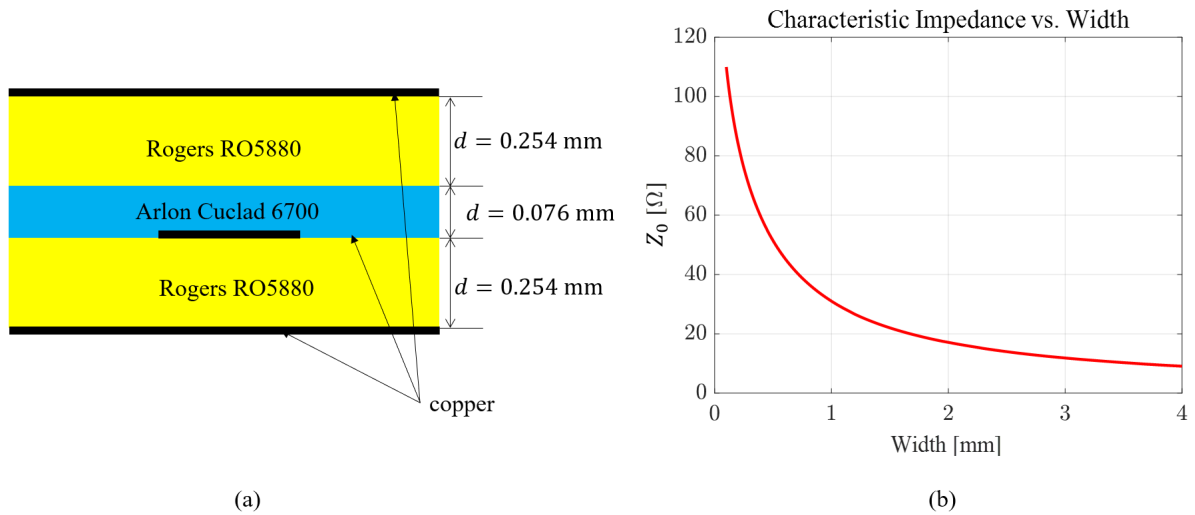


Figure 3.13: (a) Stack-up of the stripline corporate feeding network; (b) Impedance versus width of stripline.

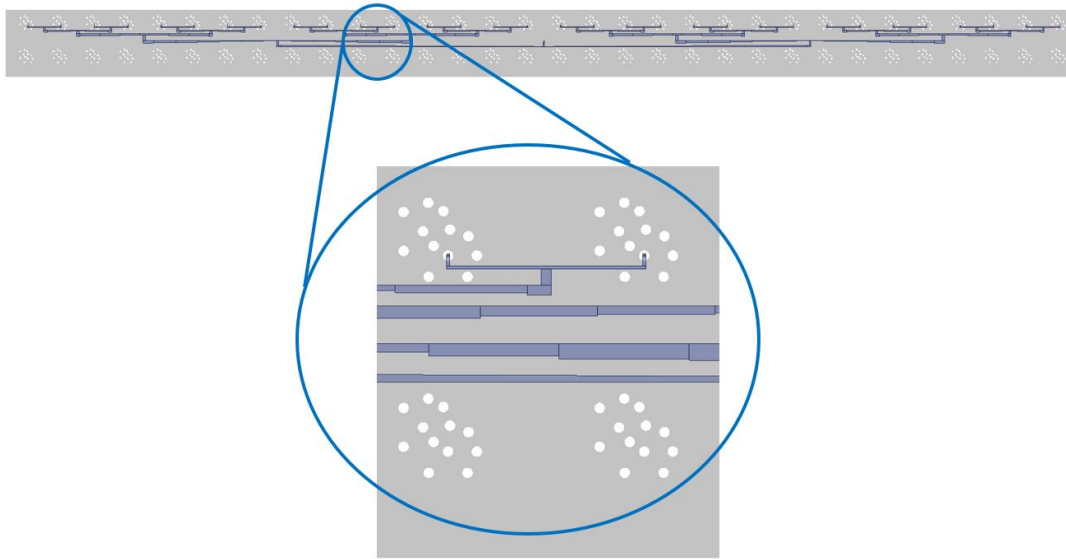


Figure 3.14: Stripline feeding network with pins allocated.

Fig. 3.16. The reflection coefficient S_{11} is lower than -15 dB over the whole band. When comparing with the microstrip, the stripline case exhibits similar losses but lower amplitude and phase variation of the output signals. This can be explained with the fact that the stripline has two ground planes above and below, thus the electric field is more confined in the surrounding of the line compared to the microstrip, reducing the cross-talk between adjacent lines.

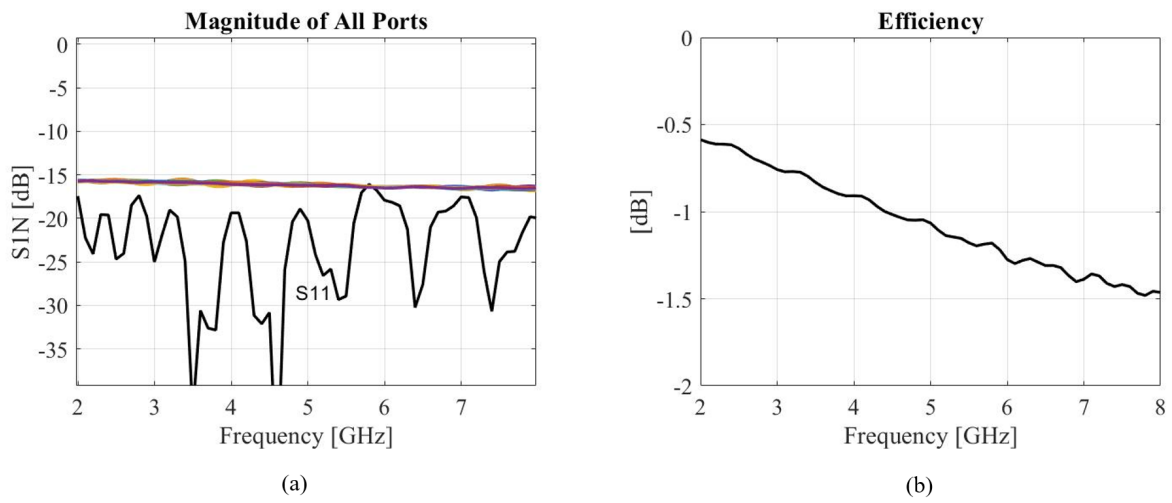


Figure 3.15: Simulated (a) S-parameters and (b) total efficiency of the 1-to-32 stripline power divider.

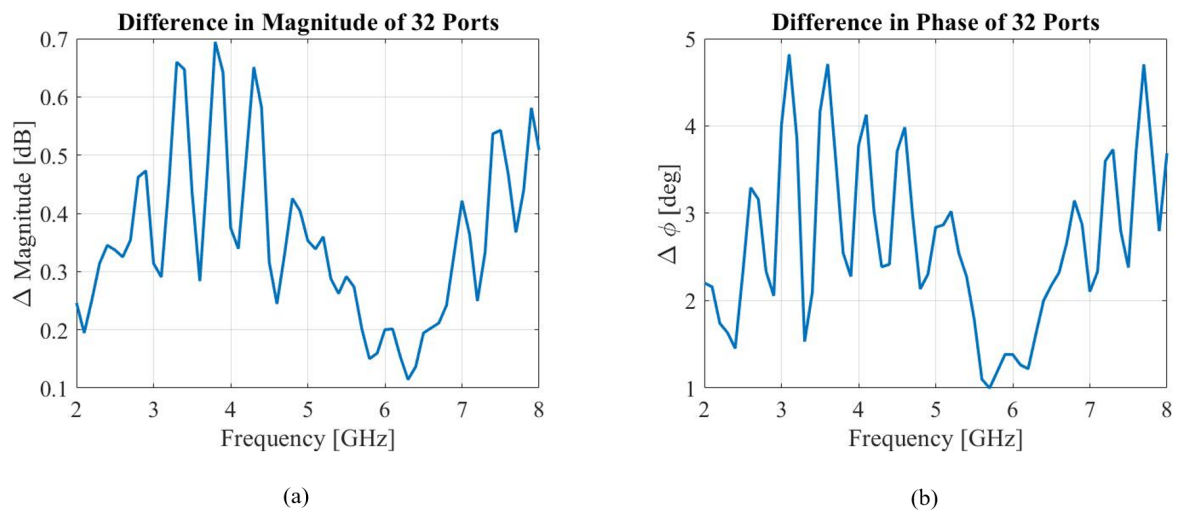


Figure 3.16: (a) Amplitude and (b) phase variation of the output ports for the 1-to-32 stripline power divider.

4

Parallel Plate Waveguide Feeding Structure

4.1. Novel Feed Concept

In this chapter, an alternative approach to feed the connected array unit cell is presented. The feed concept is based on a Parallel Plate Waveguide (PPW) structure and allows to simplify the design, with respect to the integrated coaxial feed shown in Ch. 2.

4.1.1. Drawbacks of Integrated Coaxial Feed

In connected slot array designs, the first step is to optimize the preliminary unit cell shown in Fig. 4.1(a), which includes the ADLs, an infinitely thin slot plane and a cavity below. This preliminary unit cell is simulated by means of analytical formulas without the need of a commercial software. The feed is located at the slot plane and is obtained by a constant impressed electric field distributed over a rectangular region within the slot (delta-gap generator). A realistic implementation of the feed requires to transfer the feed from the slot plane to the backing reflector, under which the coaxial connectors or the corporate feeding network are located. The typical implementation of this transition, used in all previous designs, is obtained by combining an integrated coaxial line and a microstrip, as shown in Fig. 4.1(b). The feed is now located at the ground plane and excites the vertical coaxial line and the microstrip crossing the slot and terminating with a capacitive stub. The electric field distribution in the feeding line is represented by the black arrows in the figure, to

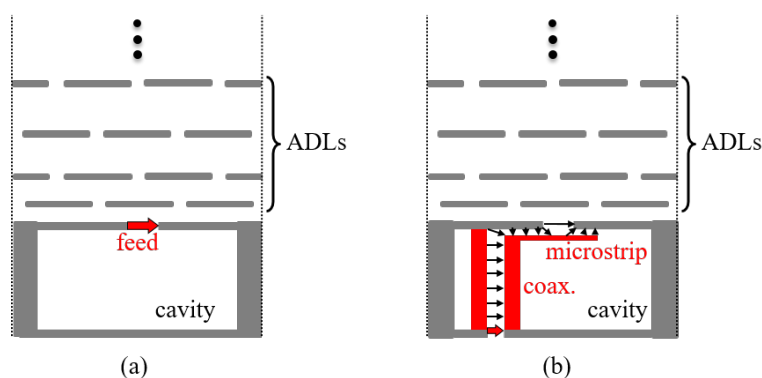


Figure 4.1: (a) Connected array unit cell with delta-gap feed at the slot plane and with (b)integrated coaxial and microstrip lines. Black arrows represent electric field distribution in the feeding lines.

highlight that the electric field propagating in the feeding lines reaches the slot to realize an approximation of the ideal delta-gap generator.

Although this strategy for the feed design was proven to be effective in Ch. 2, it has some disadvantages:

- Since the feeding structure is inside the cavity, it influences the input impedance of the slot, which changes depending on the position of the coaxial line. This requires a lengthy re-optimization of the unit cell performance when the feed is included.
- When considering a dual-polarized unit cell, two of such feeding structures should fit within a unit cell. This poses a limit on the size and the number of vias that can be allocated without degrading the array matching performance, since a large number of metal vias in the cavity yield a very low impedance of the slot.
- To reduce the number of vias, typically the coaxial lines are not fully shielded, but the outer conductors are only a semi-circle. However, this creates some coupling between the two orthogonal feeds, which can increase the cross polarization.
- To avoid too large coaxial lines, the aspect ratio of vias (length divided by diameter) needs to be as large as possible. However, this approach limits the scalability to higher frequency.

4.1.2. PPW Feed

An alternative strategy for the feed design is introduced here that simplifies the unit cell. The different logical steps that lead to the feed concept are described in Fig. 4.2.

The initial structure is the same ideal unit cell as considered early, shown again in Fig. 4.2(a). It is assumed that the ADL superstrate is composed of two quarter wave slabs, with effective medium impedances equal to Z_1 and Z_2 , respectively. The two ADL slabs implement a transformer between the free-space impedance and a lower impedance Z_L , so that the slot input impedance is well matched to Z_L . One can imagine to place a PPW section between the cavity and the ADL, with a characteristic impedance $Z_0 = Z_L$ (Fig. 4.2(b)). In

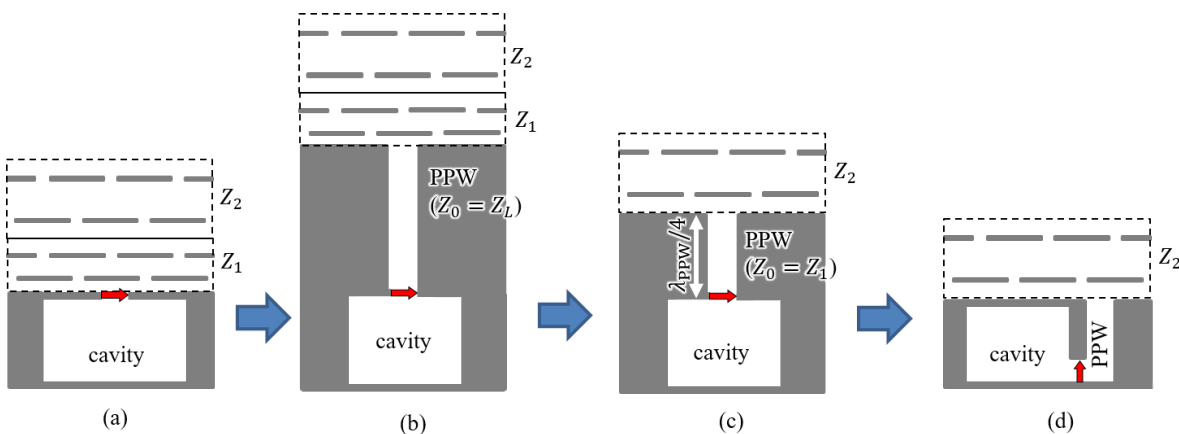


Figure 4.2: (a) Initial unit cell, with two ADL slabs; (b) PPW section included above the slot with characteristic impedance $Z_0 = Z_L$; (c) PPW section with characteristic impedance $Z_0 = Z_1$ replacing one ADL slab; (d) Folded PPW with cavity on the side and vertical feed above the ground plane.

this configuration, the slot is no longer present and the feed is located at the bottom of the PPW. The next step is to replace the lower ADL slab, with effective medium impedance Z_1 , with the PPW section, whose characteristic impedance is now $Z_0 = Z_1$. The resulting unit cell is shown in Fig. 4.2(c). The impedance transformer that before was implemented by the two ADL slabs is now realized by the ADL and the PPW. The final step consists of folding the structure as depicted in Fig. 4.2(d), so that the cavity is beside the PPW and the feed is now vertically oriented.

By comparing the structure in Fig. 4.2(d) with the previous one in Fig. 4.1(b), a number of advantages can be pointed out:

- Unlike the coaxial line, the PPW is separated from the cavity, which allows to decouple the effects of the cavity and the feed lines on the impedance of the slot.
- Since part of the ADL transformer is implemented in the PPW, the number of ADL layers is reduced, which is beneficial for cost and complexity of manufacturing.
- The PPW structure allows the realization of the vertical walls with larger vias, improving the scalability to high frequency.

To assess the effectiveness of the proposed feeding structure, two design examples are presented. The first example is a 2:1 linearly polarized connected array suitable for automotive radar applications, covering the bandwidth between 70 and 140 GHz (Sec. 4.2). A second example targets the same 4:1 bandwidth as the connected array in Sec. 4.3, from 2 to 8 GHz, with the aim to compare the current design with the one based on the integrated coaxial feed.

4.2. Example: 70 to 140 GHz Linearly Polarized Array

This example considers a single-polarized connected slot array with ADL superstrate and PPW feed, operating from 70 to 140 GHz, which covers the two frequency bands for automotive radars [46, 47]. The design procedure is described with a step-by-step approach, to provide guidelines that can be used for later designs, for example for the 2 to 8 GHz case.

4.2.1. Artificial Dielectric Design

The first step of the ADL design is the design of a transmission line impedance transformer. To transform from the characteristic impedance of free space $\zeta_0 = 377 \Omega$ to an impedance $Z_L = 50 \Omega$ with a good reflection coefficient for a 2:1 frequency band, a 2-order Chebyshev transformer can be considered. The design of this transformer follows the process introduced in Sec. 3.1. The transmission line model and reflection coefficient $\Gamma = (Z_{in} - Z_L)/(Z_{in} + Z_L)$ of this 2-section transformer is shown in Fig. 4.3.

The transmission line model can be used to represent the propagation of the fundamental Floquet wave from the array through the artificial dielectrics. For the sake of simplicity, the ADL slabs are first considered as homogeneous anisotropic dielectrics. Using the *ADL Analytical Tool* [48], one can find some realistic values of the tensor permittivity and permeability that can be achieved with ADL slabs design. The two-slab transformer has been simulated in *CST DESIGN ENVIRONMENT* for a single plane wave impinging from broadside as shown in Fig. 4.4(a), leading to the reflection coefficient shown in Fig. 4.4(b). It can be seen that it has nearly the same performance as the ideal transformer. The electrical and geometrical parameters of the two slabs are reported in Table 4.1.

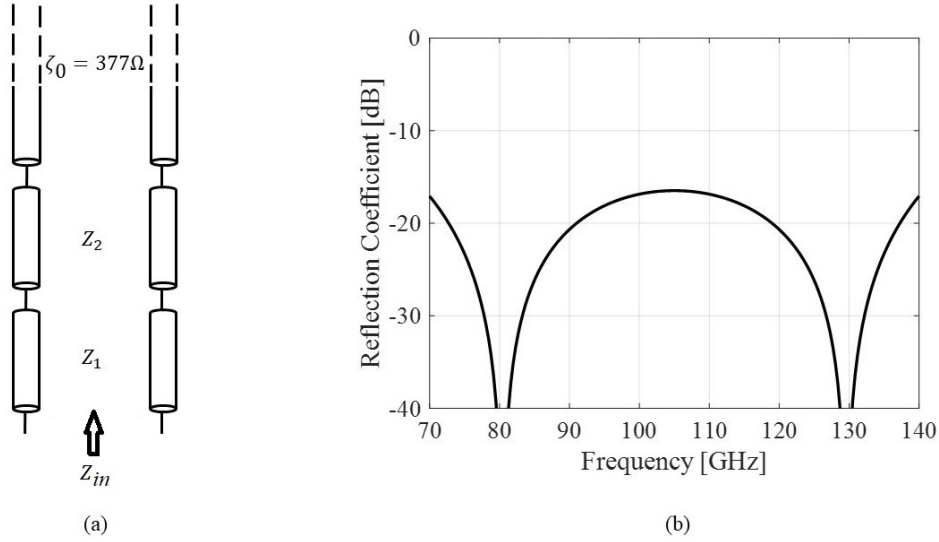


Figure 4.3: (a) Transmission line model of the two-section Chebyshev transformer; (b) Reflection coefficient.

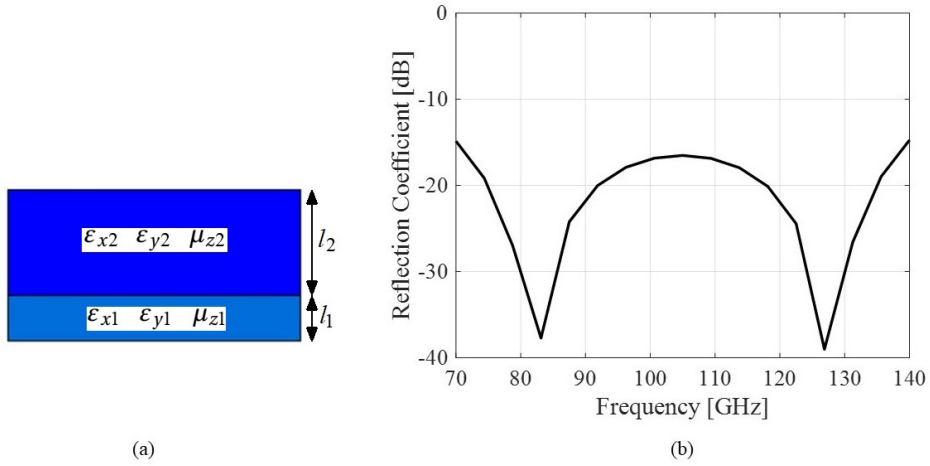


Figure 4.4: (a) Model of the two anisotropic slabs under plane wave incidence; (b) Reflection coefficient.

$\epsilon_{x1} = \epsilon_{y1}$	μ_{z1}	l_1 [mm]	Z_1 [Ω]	$\epsilon_{x2} = \epsilon_{y2}$	μ_{z2}	l_2 [mm]	Z_2 [Ω]
17.8	0.11	0.17	89.3	3.19	0.47	4.03	211.1

Table 4.1: Anisotropic slab parameters for the 2-section Chebyshev transformer. All other parameters of the tensors are $\epsilon_z = \mu_x = \mu_y = 1$ for both slabs.

4.2.2. Array Fed with a Straight PPW

Once the ADL slabs are designed, the unit cell of the array is included, made by a PPW with the same characteristic impedance as the target input impedance of the two-section transformer, which is $50\ \Omega$. The resulting unit cell is shown in Fig. 4.5(a). The PPW is fed by a delta-gap generator and a square cavity is considered below. It is assumed that both the PPW and the cavity are filled with a dielectric with relative permittivity $\epsilon_r = 2.2$, and the period of the array $d_x = d_y = 1.1\ \text{mm}$, i.e. about half wavelength at highest frequency of operation (140 GHz).

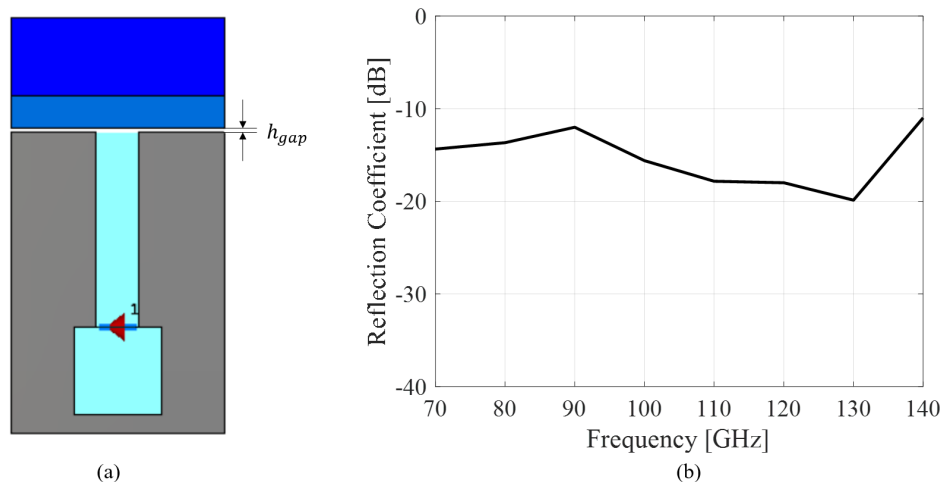


Figure 4.5: (a) Side view of the unit cell with the PPW section with characteristic impedance $Z_0 = Z_L$; (b) Active reflection coefficient.

The characteristic impedance of the PPW is given by

$$Z_0 = \zeta \frac{d}{w}, \quad (4.1)$$

where ζ is the intrinsic impedance of the dielectric material filling the PPW ($\zeta = 120\pi/\sqrt{\epsilon_r}$), and d is the distance between the two walls of the PPW. w is the width of the PPW, in this case equivalent to the period of the unit cell $w = d_x$. According to (4.1), we can calculate that the distance d of the PPW to give 50Ω characteristic impedance is 0.216 mm .

Below the PPW, a cavity with height slightly smaller than $\lambda_d/4 \approx 0.45 \text{ mm}$ (λ_d is the wavelength in the dielectric at center frequency of 105 GHz) is present, so that the impedance seen by the feed for the structure below is high compared to the impedance seen for the structure above. By optimizing the size of the feed, the air gap between the open end of the PPW and the anisotropic superstrate (h_{gap}), the active reflection coefficient in Fig. 4.5(b) is obtained, which is lower than -10 dB over the entire band of interest.

If the impedance of the PPW is chosen as the same as the impedance of the first section of the superstrate transformer, one can replace the dielectric slab with the PPW. In this case, the characteristic impedance of the PPW $Z_0 = Z_1 = 89.3 \Omega$ and $d = 0.386 \text{ mm}$ from (4.1). The length of the PPW is selected as $\lambda_d/4 = 0.48 \text{ mm}$ to behave as a section of the transformer. The model is shown in Fig. 4.6(a) and the active reflection coefficient is in Fig. 4.6(b), where a -10 dB bandwidth is achieved over the entire band.

4.2.3. Array Fed with a Folded PPW

When the cavity is below the PPW, the total height of the unit cell feed is about half wavelength. In order to reduce this height, the cavity can be folded, as shown in Fig. 4.7(a). The cavity and the PPW are placed next to each other with the feed oriented vertically in between. Fig. 4.7(b) shows the active reflection coefficient from the given unit cell, which is again lower than -10 dB over the band.

In the current unit cell, all the vertical metal walls are composed by solid metal blocks. To make it compatible with PCB manufacturing, the metal walls can be replaced by vias. The side and three-dimensional (3-D) views of the slot structure with solid metal and with

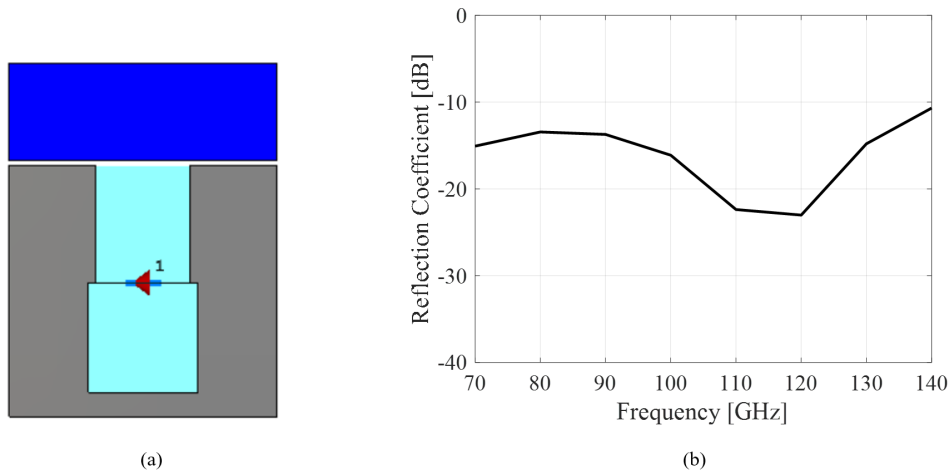


Figure 4.6: (a) Side view of the unit cell with $Z_0 = Z_1$ to replace one ADL slab; (b) Active reflection coefficient.

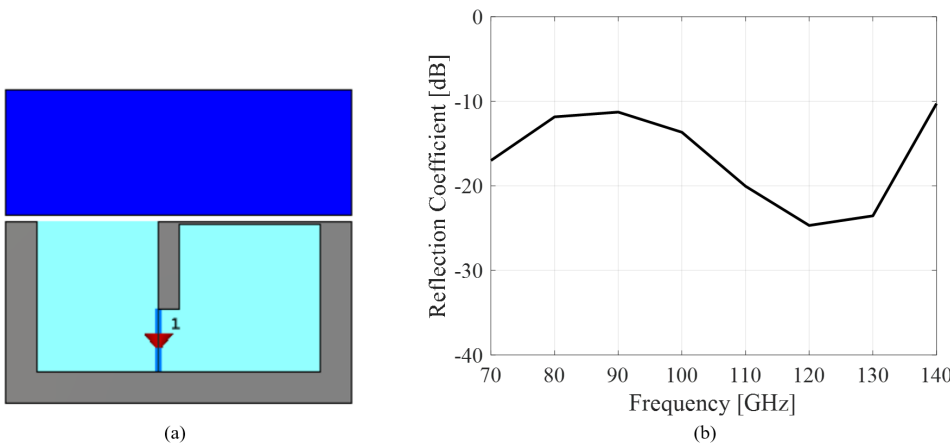


Figure 4.7: (a) Side view of the unit cell with with folded feed; (b) Active reflection coefficient.

vias are shown in Fig. 4.8. The side walls of the unit cell are realized with vias connecting the slot plane with the backing reflector. The other wall of the PPW is obtained with vias that start from the slot plane but stop at an intermediate layer, without reaching the ground plane. Only one of such vias acts as the feed and is made longer to cross the ground plane through a circular opening and to reach the microstrip feeding line underneath the ground plane.

For the unit cell design, the via diameter is 0.1 mm and the pitch between vias (center-to-center) is 0.23 mm. Via pads are included with the diameter of 0.26 mm. A central pin is directly connected with a microstrip through a hole on the ground plane to give a characteristic impedance of 50 Ω . The width of the microstrip is 0.36 mm and it is on a substrate with $\epsilon_r = 2.2$, thickness = 0.127 mm. The edge-to-edge distance for the vias in the PPW is $d = 0.4$ mm.

4.2.4. Array Unit Cell with ADLs

The last step to complete the design is replacing the homogeneous anisotropic slab with real ADL patches. Using the *ADL Analytical Tool* [48], the ADL is designed. It is a two-layer ADL with dielectric with relative permittivity $\epsilon_r = 2.2$ between the layers. The model is

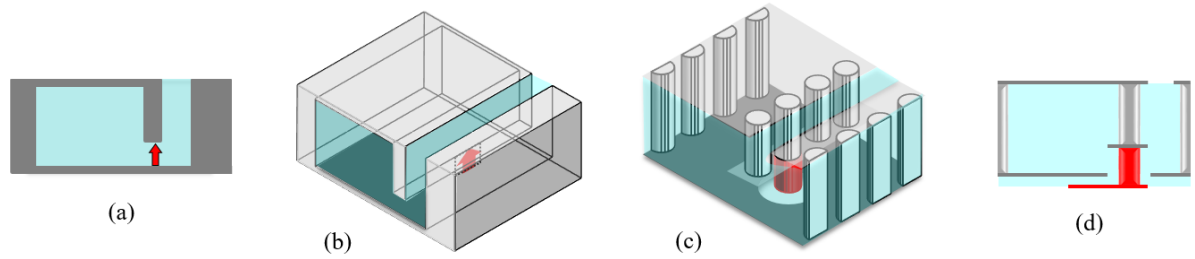


Figure 4.8: (a) Side-view and (b) 3-D view of the array element, with metal blocks and ideal lumped feed; (c) 3-D view and (d) Side-view of the array element, with vias replacing the metal walls and the feed. The feeding via crosses the ground plane through a hole to connect with a microstrip line.

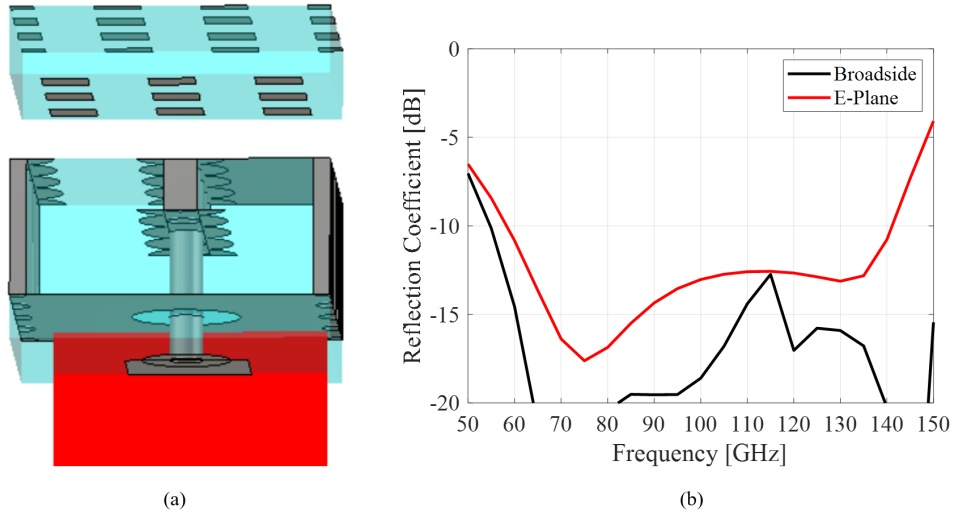


Figure 4.9: (a) Unit cell model with feed and ADLs; (b) Active reflection coefficient for broadside and scanning to 60° in the E-plane.

shown in Fig. 4.9(a). Besides broadside, for an automotive radar, a good performance for scanning in one plane is also expected. Figure 4.9(b) shows that this model has a reflection coefficient lower than -10 dB over the band from 60 to 141 GHz, not only for broadside, but also for E-plane scanning up to 60° . This design has potential for application in dual-band automotive radar covering simultaneously the bands around 79 GHz and 140 GHz.

4.3. Example: 2 to 8 GHz Array

As a second example, the same design procedures can be applied for an array operating at 2-8 GHz. This will allow to compare the performance and the complexity of the unit cell with respect to the previous design based on the integrated coaxial feed.

4.3.1. Artificial Dielectric Design

The first step is to design dielectric slabs that provide good matching over the operation frequency. To transform the free-space impedance $\zeta_0 = 377 \Omega$ to $Z_L = 50 \Omega$ with a good reflection coefficient for a 4:1 frequency band, a 4-order Chebyshev transformer can be implemented. Because the maximum frequency of operation (8 GHz) is more critical to match, the Chebyshev response is centered at 6 GHz instead of 5 GHz, to provide some margin for matching in the high end of the band. The reflection coefficient of this 4-section

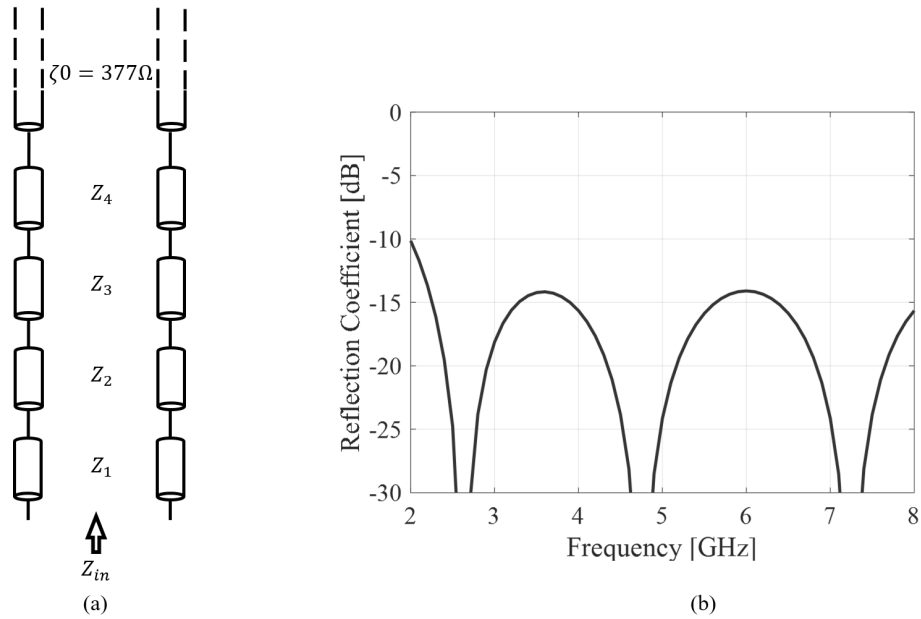


Figure 4.10: (a) Transmission line model of the four-section Chebyshev transformer; (b) Reflection coefficient.

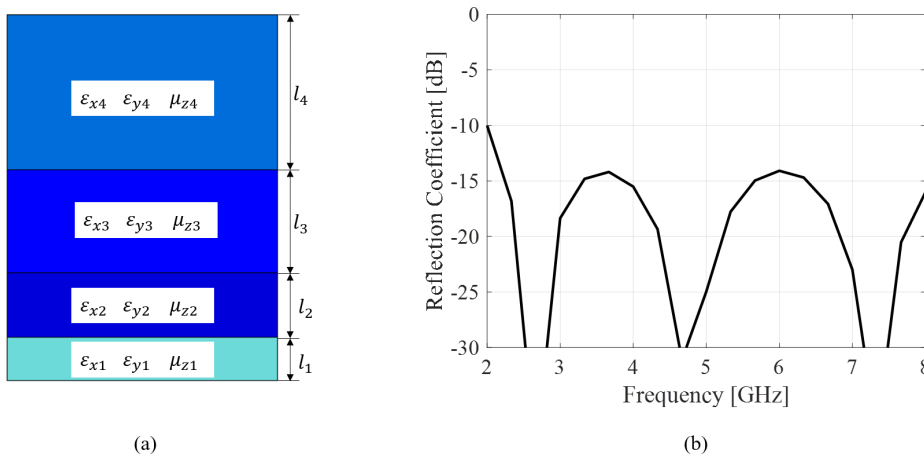


Figure 4.11: (a) Model of the four anisotropic slabs under plane wave incidence; (b) Reflection coefficient.

transformer is shown in Fig. 4.10. The electrical and geometrical parameters of the four slabs are reported in Table 4.2.

With these parameters, a model with 4-layer dielectric slabs is implemented in *CST STUDIO SUITE*, as shown in Fig. 4.11(a). Considering a plane-wave illumination on the slabs and renormalizing to the correct impedances, the reflection coefficient is shown in Fig. 4.11(b). It can be seen that it has nearly the same response as the ideal transformer.

4.3.2. Array Fed with a Straight PPW

The next step is to design the connected array unit cell. As shown in Sec. 2.2, having a larger permittivity for the host medium in the first slab has a positive effect on the active matching when scanning in the E-plane. Therefore, the value $\epsilon_{z1} = 2.2$ instead of 1 is assumed for the lowest dielectric slab.

$\epsilon_{x1} = \epsilon_{y1}$	μ_{z1}	l_1 [mm]	Z_1 [Ω]	$\epsilon_{x2} = \epsilon_{y2}$	μ_{z2}	l_2 [mm]	Z_2 [Ω]
26.8	0.14	2.4	72.8	11.9	0.15	3.6	109.1

$\epsilon_{x3} = \epsilon_{y3}$	μ_{z3}	l_3 [mm]	Z_3 [Ω]	$\epsilon_{x4} = \epsilon_{y4}$	μ_{z4}	l_4 [mm]	Z_4 [Ω]
4.8	0.34	5.7	172.8	2.1	0.64	8.6	259.1

Table 4.2: Anisotropic slab parameters for the 4-section Chebyshev transformer. All other parameters of the tensors are $\epsilon_z = \mu_x = \mu_y = 1$ for the slabs.

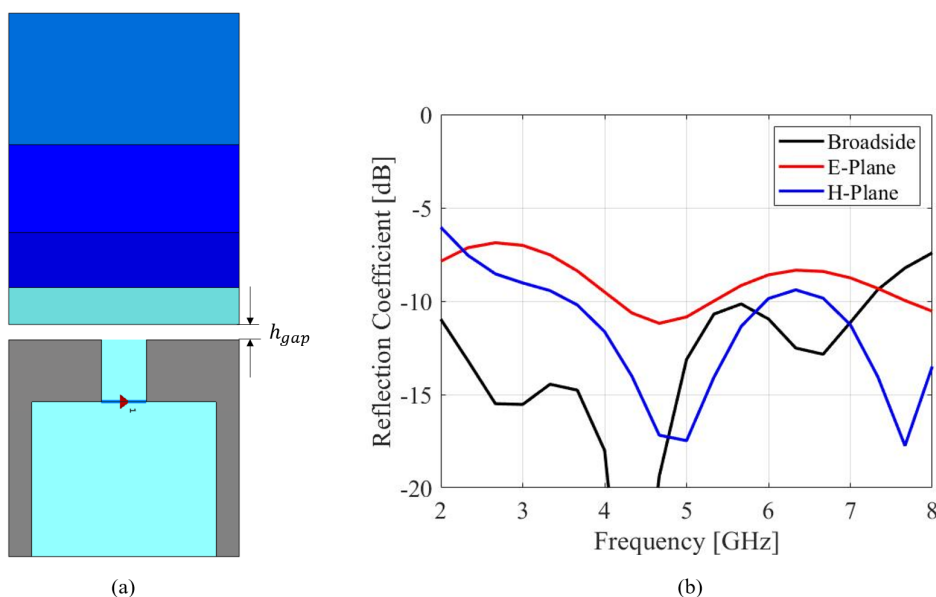


Figure 4.12: (a) Side view of the unit cell with the PPW section with characteristic impedance $Z_0 = Z_L$, (b) Active reflection coefficients for the unit cell for broadside and scanning up to 60° in E- and H-planes.

A PPW section is included, with the same impedance as the value seen for the dielectric stratification above the array (50Ω). It is assumed that the PPW is filled with the substrate with $\epsilon_r = 2.2$, and the period is the same as the design in Ch. 2, i.e. $d_x = d_y = 15$ mm. According to (4.1), the distance d of the PPW is 2.95 mm to obtain a characteristic impedance of 50Ω . Below the PPW, there is a cavity with height of about $\lambda_d/4 = 10$ mm, where λ_d is the wavelength in the dielectric at the central frequency of 5 GHz.

After some fine tuning, the model in Fig. 4.12(a) is obtained. The active reflection coefficients are shown in Fig. 4.12(b), for radiation to broadside as well as for scanning in E- and H- planes up to 60° . It can be seen that for broadside, reflection coefficient is lower than -10 dB for most of the band, and it is lower than -6 dB for both scanning cases, which corresponds to an active voltage standing wave ratio $VSWR < 3$.

Following the design procedure, the impedance of the PPW is now made the same as the impedance of the first section of the transformer, so that we can replace one dielectric slab with the PPW. In this case, the characteristic impedance of the PPW $Z_0 = Z_1 = 72.8 \Omega$, and $d = 4.3$ mm. The length of the PPW should be around $\lambda_d/4 = 10$ mm to behave as a

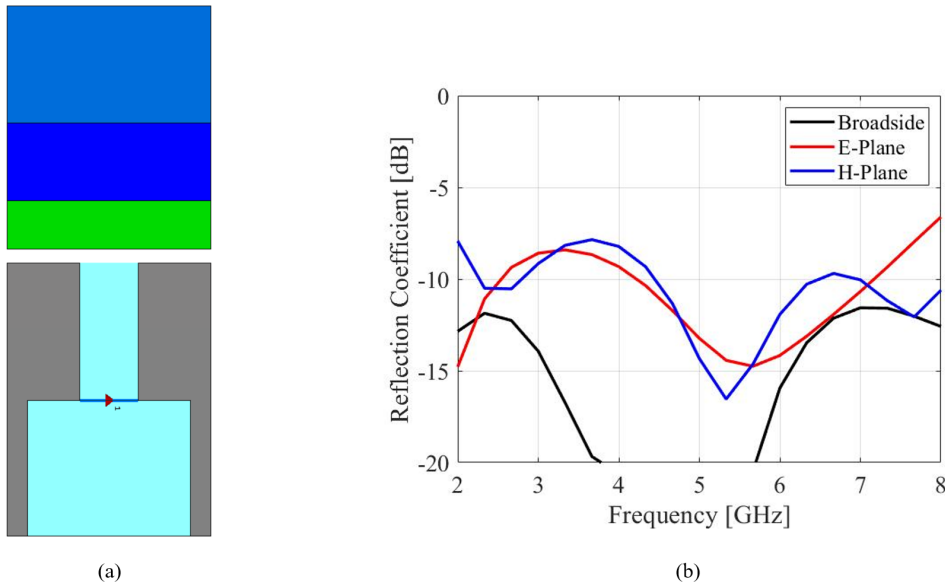


Figure 4.13: (a) Side view of the unit cell with $Z_0 = Z_1$ to replace one ADL slab; (b) Active reflection coefficients for the unit cell for broadside and scanning up to 60° in E- and H-planes.

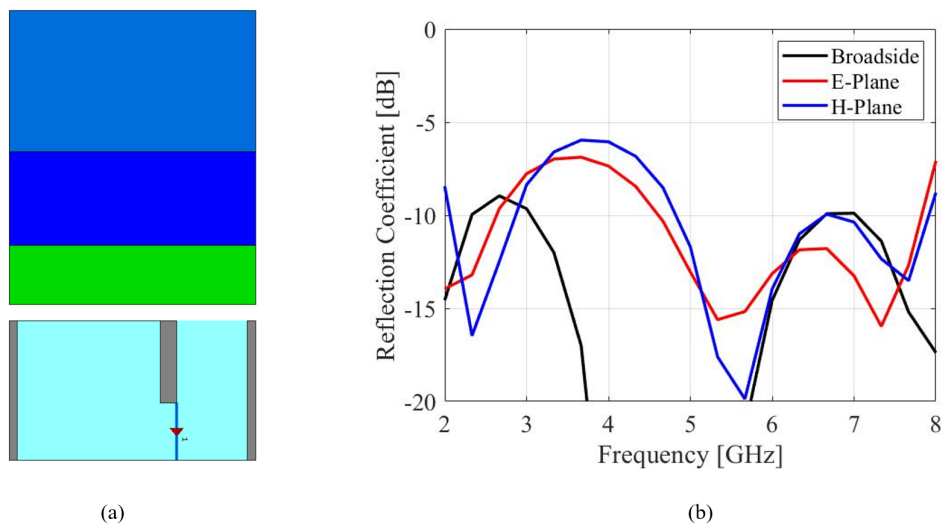


Figure 4.14: (a) Side view of the unit cell with folded feed; (b) Active reflection coefficients.

section of transformer. Since now the second slab of the original dielectric superstrate is shifted down to become the first layer closest to the array, the z -component of the relative permittivity tensor is assumed to be $\epsilon_z = 2.2$ instead of 1. This can be obtained with an ADL slab where the patches are embedded in a host medium with $\epsilon_r = 2.2$.

The side view of the resulting unit cell is shown in Fig. 4.13(a) and the active reflection coefficients are in Fig. 4.13(b). It can be seen that for broadside, reflection coefficient is lower than -10 dB for the entire band, and it is lower than -7 dB for scanning in both main planes to 60° .

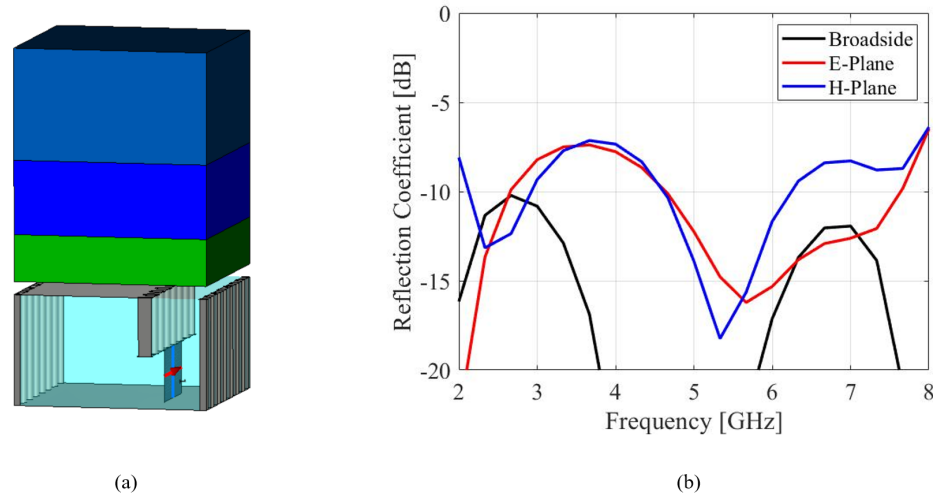


Figure 4.15: (a) Unit cell model with folded feed with pins and discrete port; (b) Active reflection coefficients for the unit cell for broadside and scanning up to 60° in E- and H-planes.

4.3.3. Array Fed with a Folded PPW

The next step is to fold the cavity to reduce the total height of slot array, as shown in Fig. 4.14(a). The reflection coefficients are shown in Fig. 4.14(b), which is lower than -10 dB for the most band for broadside and lower than -6 dB for scanning in both main planes to 60° .

Finally, the metal blocks can be replaced by plated-through vias. The total height of the substrate is 8.5 mm, thus considering 8:1 aspect ratio, the diameter of vias is 1 mm. The edge-to-edge distance between two adjacent vias is 1.14 mm. For the PPW section, the edge-to-edge distance between the two via walls is $d = 3.8$ mm. After some tuning, the model and reflection coefficients are shown in Fig. 4.15.

To make the feed more realistic, the delta-gap source is changed into a realistic feed, which is a central pin directly reaching the ground plane through a hole, fed by a waveguide port. Comparing with the discrete port, the feeding via is much thinner, which yields an increased inductance. In order to compensate for this, in post processing, a 3 pF series capacitor is included. Moreover, a resonance was observed at around 8 GHz when scanning to 60° in the H-plane. To shift this resonance to higher frequency, the dielectric material near the central pin is removed, similarly to the perforated dielectric grid used in Ch. 2. Figure 4.16(a) and (b) show the CST model and the active reflection coefficients normalized to 75Ω , respectively.

4.3.4. Array with ADLs

To complete the single-polarized design, the homogeneous slabs are replaced with the real ADLs. The *ADL Analytical Tool* [48] can only be used to design ADL for single slab because it does not consider the interaction between layers of different slabs. For this reason, the initial parameters derived from the tool are tuned to account for the interaction between slabs. In order to design the ADL, the method in [35] is employed. The ADL synthesis starts with simulating the reflection and transmission parameters of the three dielectric slabs under plane-wave incidence. Then, a MATLAB code is implemented to analytically simulate a 6-layer ADL. The code is run many times in an optimization procedure, to design the ADL to have similar response as the slabs.

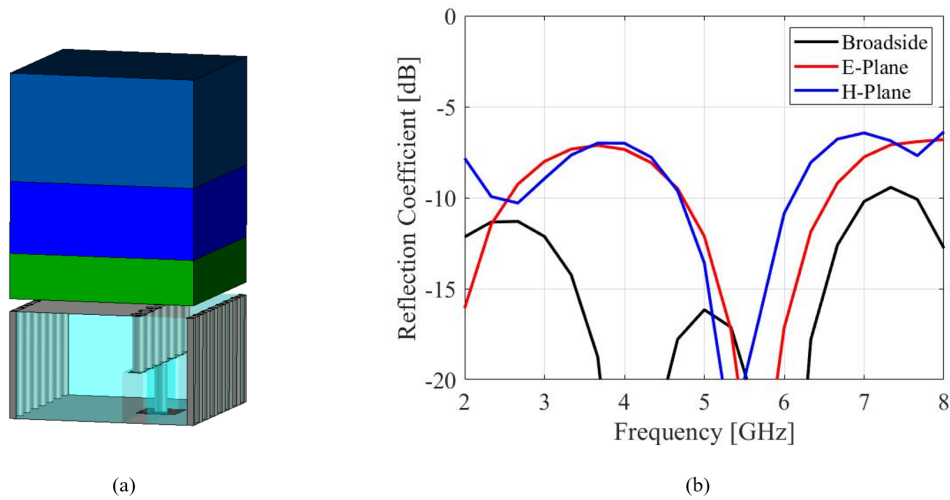


Figure 4.16: (a) Unit cell model with folded feed with pins and waveguide port; (b) Active reflection coefficients for the unit cell for broadside and scanning up to 60° in E- and H-planes.

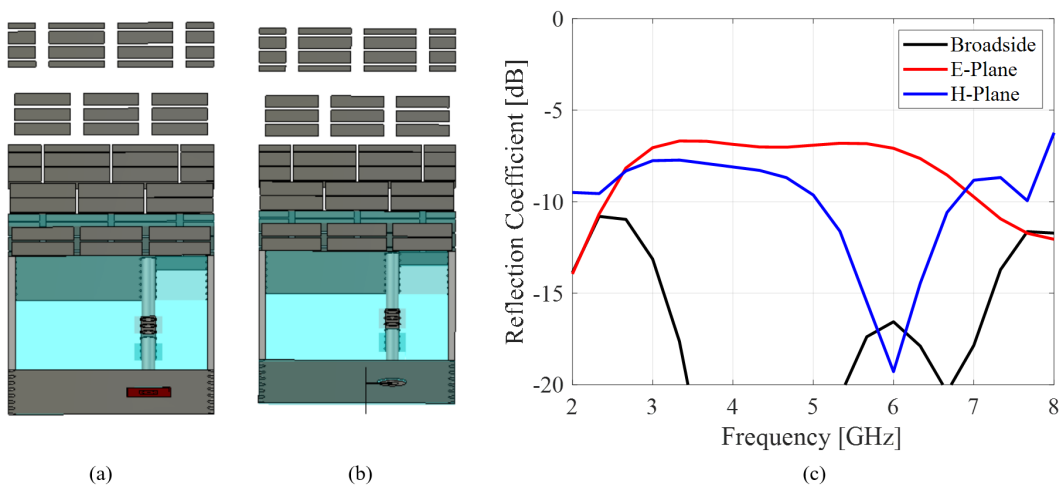


Figure 4.17: (a) Unit cell model with ADL; (b) Unit cell model with ADL and microstrip feed; (c) Active reflection coefficients for the unit cell for broadside and scanning up to 60° in E- and H-planes.

Placing the designed ADL above the array with the certain distance leads to the final model of the unit cell shown in Fig. 4.17(a). Finally, the feeding via is connected to a microstrip line below the ground plane as in Fig. 4.17(b). The microstrip has a width of 0.13 mm and is printed on a substrate with thickness 0.127 mm and relative dielectric constant $\epsilon_r = 2.2$. The active reflection coefficients are reported in Fig. 4.17(c), which shows values lower than -10 dB for broadside, and lower than -6 dB for scanning to 60° in the E- and H-planes.

4.4. Array for Dual Polarization

The feed concept presented in this chapter was thus far only designed in a single-polarized unit cell. However, to compare with the previous design based on integrated coaxial feed, the PPW-based structure needs to be compatible with a dual-polarized array configuration.

To achieve the two orthogonal polarizations, the single polarized unit cell in Fig. 4.18(a)

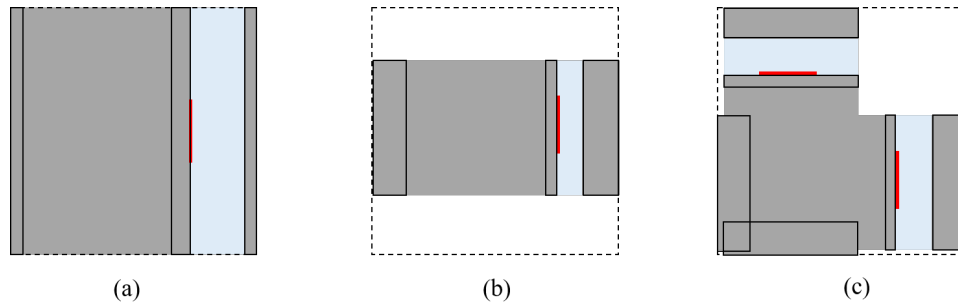


Figure 4.18: (a) Top view of the single polarized connected PPW array; (b) Reduction of the PPW size; (c) Dual-polarized configuration.

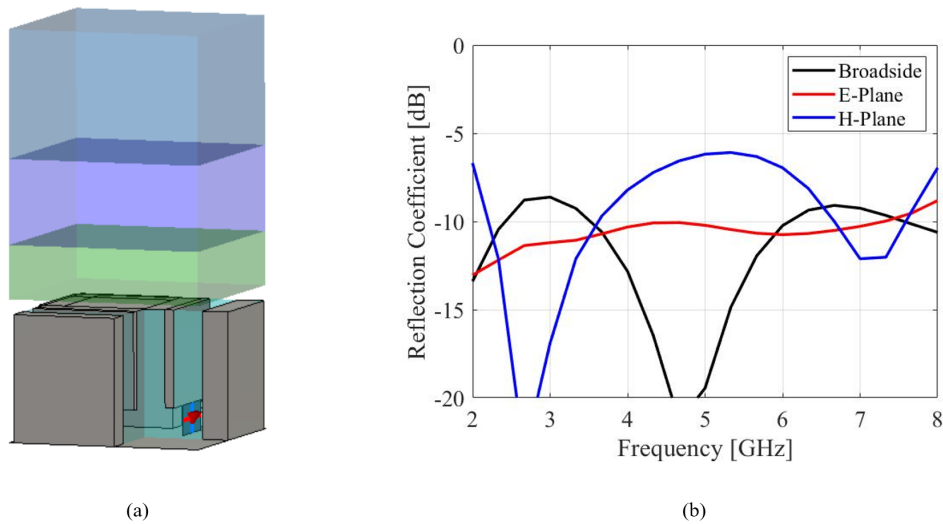


Figure 4.19: (a) Unit cell model with dual-polarized feed; (b) Active reflection coefficients for the unit cell for broadside and scanning up to 60° in E- and H-planes.

is first converted in the structure shown in Fig. 4.18(b), where the size of the PPW is reduced by about half. One can note that the latter configuration resembles a connected dipole array, instead of the connected slot. The narrower structure can be duplicated for the orthogonal element to achieve double polarizations, as depicted in Fig. 4.18(c). To improve the matching, the dielectric is removed in the region outside the cavity and PPW, realizing a dielectric grid.

The performance of the unit cell is presented in Fig. 4.19. A 3 pF series capacitor is added in post processing, to improve the matching. It can be observed that the active reflection coefficient remains below -6 dB for scanning to broadside and to 60° in the E- and H-planes.

The next step is to replace the solid metal blocks of the unit cell with vias. The 3-D and side views of the unit cell structure with vias are shown in Fig. 4.20. The side walls of the unit cell are realized with vias connecting the slot plane with the backing reflector. The other walls of the PPW are obtained with vias that start from the slot plane but stop at an intermediate layer, without reaching the ground plane. Only two of such vias act as the feed and are made longer to cross the ground plane through circular opening and to reach the microstrip feeding line underneath the ground plane. For the unit cell design, the via diameter is 1 mm and via pads are included with the diameter of 0.26 mm. The width of

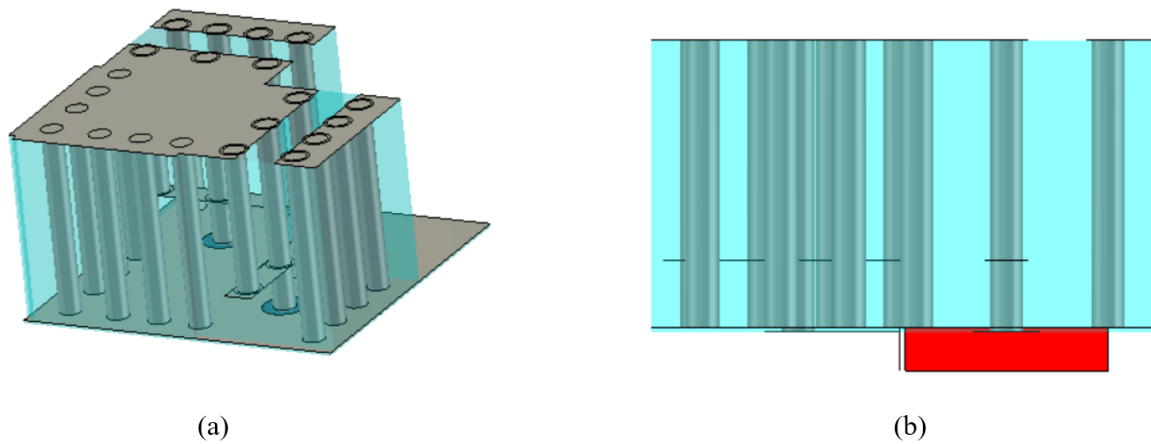


Figure 4.20: (a) 3-D view and (b) side view of unit cell with vias replacing the metal walls and the feed. The feeding via crosses the ground plane through a hole to connect with a microstrip line.

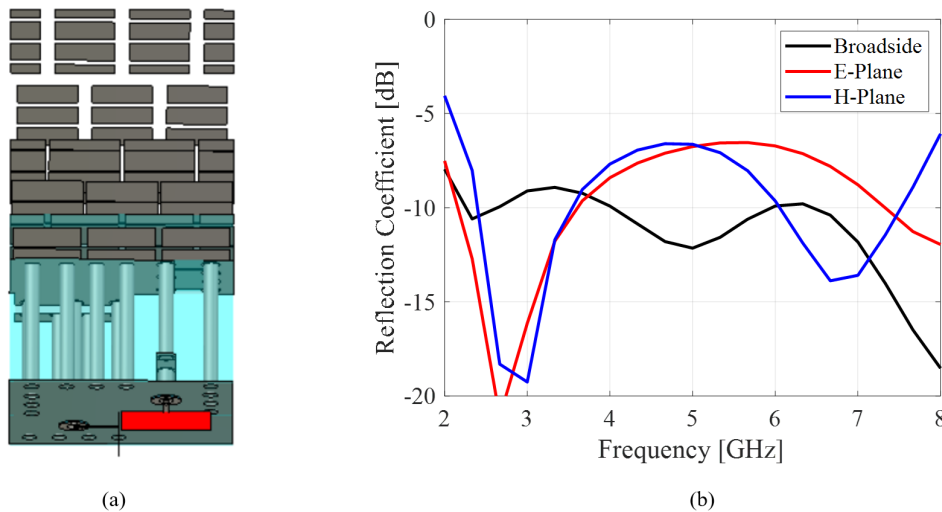


Figure 4.21: (a) Unit cell model with dual-polarized feed; (b) Active reflection coefficients for the unit cell for broadside and scanning up to 60° in E- and H-planes.

the microstrip is 0.36 mm to give a characteristic impedance of 50Ω and it is on a substrate with $\epsilon_r = 2.2$, thickness = 0.127 mm . The edge-to-edge distance for the vias in the PPW is $d = 2 \text{ mm}$.

Then the previous 6-layer ADL superstrates can be used to replace the 3-section homogeneous anisotropic slabs. The final model of the unit cell shown in Fig. 4.21(a). The active reflection coefficients are reported in Fig. 4.21(b), which shows values lower than -8 dB for broadside for the whole band from 2 to 8 GHz, and lower than -6 dB for scanning to 60° in the E- and H-planes from 2.1 to 8 GHz.

Compared with previous 2-8 GHz unit cell design, with integrated coaxial, this new feed concept has the following advantages:

1. The design procedure of a PPW and cavity is easier than that of the integrated coaxial, as there is no need to optimize the position of each via together with the slot parameters. This is due to the fact that the feed and the radiating slot design are better

decoupled, unlike the coaxial feed case.

2. The perforations in the dielectric substrate go through entire stack-up, unlike the previous design, where the dielectric grid was sandwiched between two continuous dielectric layer, leading to complex manufacturing.
3. The number of layers of the ADL is reduced from 8 to 6, because part of the impedance transformation is implemented in the PPW.

5

Conclusions and Future Work

5.1. Conclusions

The first part of the thesis described the design of an integrated coaxial feed for a dual-pol connected slot array associated with two interchangeable ADL superstrates designs, one covering from 2 to 8 GHz (WB) and the other one covering from 6 to 8 GHz (NB). The integrated coaxial feeds comprise a microstrip-to-coax-to-microstrip and a microstrip-to-coax-to-stripline transition, depending on the polarization.

For the NB ADL, the simulated active reflection coefficient was shown to be lower than -10 dB when scanning up to $\pm 60^\circ$ in every azimuthal plane, from 6 to 8 GHz. When combined with the WB ADL, an active reflection coefficient lower than -8 dB was observed for broadside, from 2.3 until 8 GHz, while a -6 dB bandwidth is achieved from 2.1 to 8 GHz for scanning up to $\pm 60^\circ$.

Besides the 32×26 element array, capable of scanning only on the main planes, a fully connectorized version of it, having 8×8 elements, was considered to achieve scanning on every azimuthal plane. For this latter case, the integrated coaxial feed is excited through an SMP connector. The matching of the unit cell of this final structure is comparable to the one of the unit cell for the 32×26 array.

The designs of a 1-to-32 corporate microstrip feeding network and a 1-to-32 corporate stripline feeding network were presented, to feed the 32×26 dual-polarized connected array. The input port has a normalization impedance of 50Ω for connecting to the coaxial cable, while the output port impedance is 85Ω and 70Ω for the microstrip and the stripline, respectively. The microstrip feeding network has a reflection coefficient lower than -14 dB over the band, and the deviation in phase and magnitude between the 32 output ports is lower than 10° and 1.25 dB, respectively. As for the stripline feeding structure, a -15 dB reflection coefficient is achieved, with maximumly 0.7 dB deviation in magnitude and 5° deviation in phase for the output ports over the band of interest.

Finally a novel feed concept was proposed, where a PPW replaces the integrated coaxial lines feeding the array. This structure simplifies the design of the connected array feed, and, since the PPW can behave as an impedance transformer in place of one ADL section, the total number of the used ADL layers can be reduced, leading to an easier and cheaper manufacturing. A first example of this concept was shown for a single-pol connected array operating between 70 to 140 GHz, exhibiting a reflection coefficient lower than -10 dB for broadside and for scanning up to 60° on the E-plane. This design has potential to be used

in dual-band automotive radars in the future. Then a PPW feed operating in dual-pol from 2 to 8 GHz is designed in combination with the slot and the wideband ADL superstrate. Comparing with the previous feed with integrated coaxial, the PPW case exhibits similar performance but it successfully reduces the number of layers of ADL from 8 to 6, because part of the impedance transformation is implemented in the PPW.

5.2. Future Work

Possible future developments related to the work described in this thesis can be the following:

Prototype measurements. The thesis presented only simulated results from the array unit cell. However, a number of prototypes based on the designs presented here are currently under manufacturing: these comprise a 32×26 antenna board (i.e. the hybrid fed array), an 8×8 antenna board (i.e. the fully connectorized array), a 4-layer radome board (i.e. NB ADL), and an 8-layer radome board (i.e. WB ADL). The details of the aforementioned boards are explained in Appendix B. After the manufacturing will have been accomplished, matching and patterns measurements will be performed.

Analytical models for the PPW-fed connected array. The spectral domain techniques customarily used to model the connected array unit cell fail to model a PPW-fed unit cell of Ch. 4, because the presence of the PPW itself changes the fields on the slot plane. Thus a new analytical model, aimed at describing such configuration, can be formalized.

PPW-fed connected array prototype. The PPW-fed connected array has been analyzed only in terms of simulations. A prototype based on such concept can be realized in the future, to experimentally validate the effectiveness of this solution.

A

Derivation of the Impedance for 5-Section Chebyshev Transformers

The expression of a n^{th} -order Chebyshev polynomial can be expressed as a function of the lower-order polynomials, using the following iterative expression:

$$T_n(x) = 2xT_{n-1}(x) - T_{n-2}(x). \quad (\text{A.1})$$

By replacing x with $\cos\theta$ for $|x| < 1$, the Chebyshev polynomial will be

$$T_n(\cos\theta) = \cos n\theta. \quad (\text{A.2})$$

Then replace $\cos\theta$ with $\sec\theta_m \cos\theta$,

$$T_n(\sec\theta_m \cos\theta) = \cos n[\cos^{-1}(\sec\theta_m \cos\theta)], \quad (\text{A.3})$$

so that for 5-section Chebyshev transformers

$$T_3(\sec\theta_m \cos\theta) = \sec^3\theta_m(\cos 3\theta + 3\cos\theta) - 3\sec\theta_m \cos\theta, \quad (\text{A.4})$$

$$T_4(\sec\theta_m \cos\theta) = \sec^4\theta_m(\cos 4\theta + 4\cos 2\theta + 3) - 4\sec^2\theta_m(\cos 2\theta + 1) + 1, \quad (\text{A.5})$$

$$T_5(\sec\theta_m \cos\theta) = 2\sec\theta_m \cos\theta T_4(\sec\theta_m \cos\theta) - T_3(\sec\theta_m \cos\theta), \quad (\text{A.6})$$

and

$$\sec\theta_m = \cosh \left[\frac{1}{5} \cosh^{-1} \left(\left| \frac{\ln(Z_L/Z_0)}{2\Gamma_m} \right| \right) \right], \quad (\text{A.7})$$

where Γ_m is the ripple of the transformer, the reflection coefficients are

$$\Gamma_5 = \Gamma_0 = \frac{1}{2} A \sec^5\theta_m, \quad (\text{A.8})$$

$$\Gamma_4 = \Gamma_1 = \frac{1}{2} A (5 \sec^5\theta_m - 5 \sec^3\theta_m), \quad (\text{A.9})$$

$$\Gamma_3 = \Gamma_2 = \frac{1}{2} A (10 \sec^5\theta_m - 15 \sec^3\theta_m + 5 \sec\theta_m), \quad (\text{A.10})$$

with $A = \Gamma_m$. The characteristic impedances of these 5 sections are

$$Z_1 = e^{\ln Z_0 + 2\Gamma_0}, \quad (\text{A.11})$$

$$Z_2 = e^{\ln Z_1 + 2\Gamma_1}, \quad (\text{A.12})$$

$$Z_3 = e^{\ln Z_2 + 2\Gamma_2}, \quad (\text{A.13})$$

$$Z_4 = e^{\ln Z_3 + 2\Gamma_3}, \quad (\text{A.14})$$

$$Z_5 = e^{\ln Z_4 + 2\Gamma_4}. \quad (\text{A.15})$$

Finally, the total reflection coefficient can be expressed as

$$\Gamma = Ae^{-5j\theta} T_5(\sec\theta_m \cos\theta). \quad (\text{A.16})$$

B

Prototype of the Final Board Design

B.1. Antenna Boards

After having introduced the integrated coaxial feed, the details of the final antenna printed circuit board are defined. However, the biggest size of dielectric Rogers 5880 is 610 mm×457 mm, which is not big enough for 32×32 elements, so it has been decided to have a slightly smaller array, with 32×26 elements that also behaves good enough for applications. The antenna boards are depicted in Fig. B.1 and consist of two boards for the antennas, one for the large array with 32×26 elements and one for the small 8×8 array.

The ADL radomes are also of two types, for the NB and WB designs, respectively. The stack-ups of the two array boards are shown in Fig. B.2 and Fig. B.3, with details of the dielectric and metal layers, including the thickness. The stack-ups of the two boards are not the same, since the first array includes the stripline layer, while the small array only considers the microstrip layers for both ports, terminated with the SMP connectors. The array part, consisting on layers M1 and M2 does not differ between the two boards. The 32×26 array board uses layer M3 as a ground plane, layer M4 for the stripline corporate feeding network and via pads, layer M5 as a ground plane and layer M6 for the microstrip corporate feeding network and for the footprint of the SMP connectors. On the contrary, the 8×8 array uses M3 for the via pads, M4 as the ground plane and M5 for the microstrip and the footprint of the SMP connectors.

Figure B.4 shows some details of the array plane and the dielectric grid for the 26×32 connected array (both in common with the 8×8 array), and the microstrip and stripline feeding networks, overlaid in the same figure. The dielectric grid is realized with a milled dielectric, needed to sustain the structure and to allow the support for the vias. The stripline feeding network, which is located on M4, is connected to M6 using vias to reach the SMP connector layer.

B.2. Radome Boards

Figure B.5 and Figure B.6 show the full stack-ups with the thicknesses and the arrangements of the materials for the WB and NB ADL boards, respectively, according to the optimization performed in Sec. 2.2. The minimum thickness of the foam layers is kept at 500 μm, which is the minimum allowed by the manufacturing process.

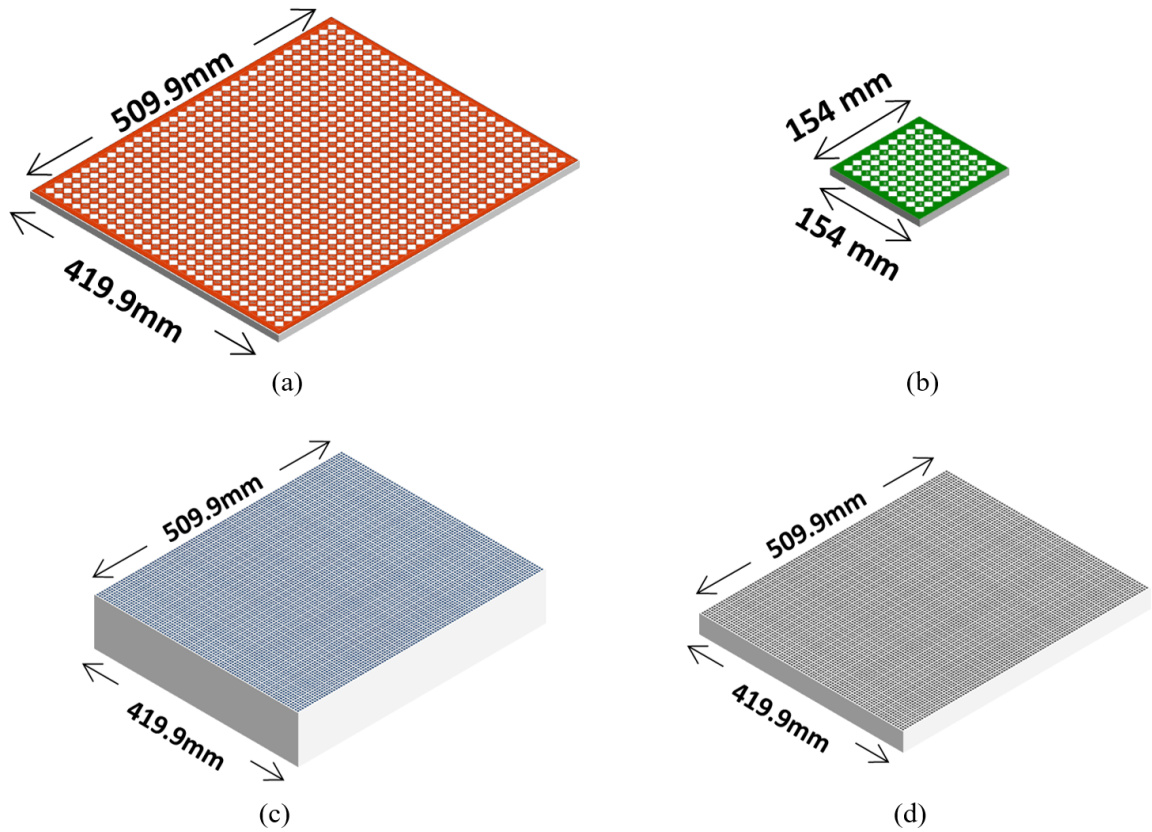


Figure B.1: Sketch of the (a) 32×26 -element antenna board, (b) 8×8 -element antenna board, (c) WB ADL board, and (d) NB ADL board.

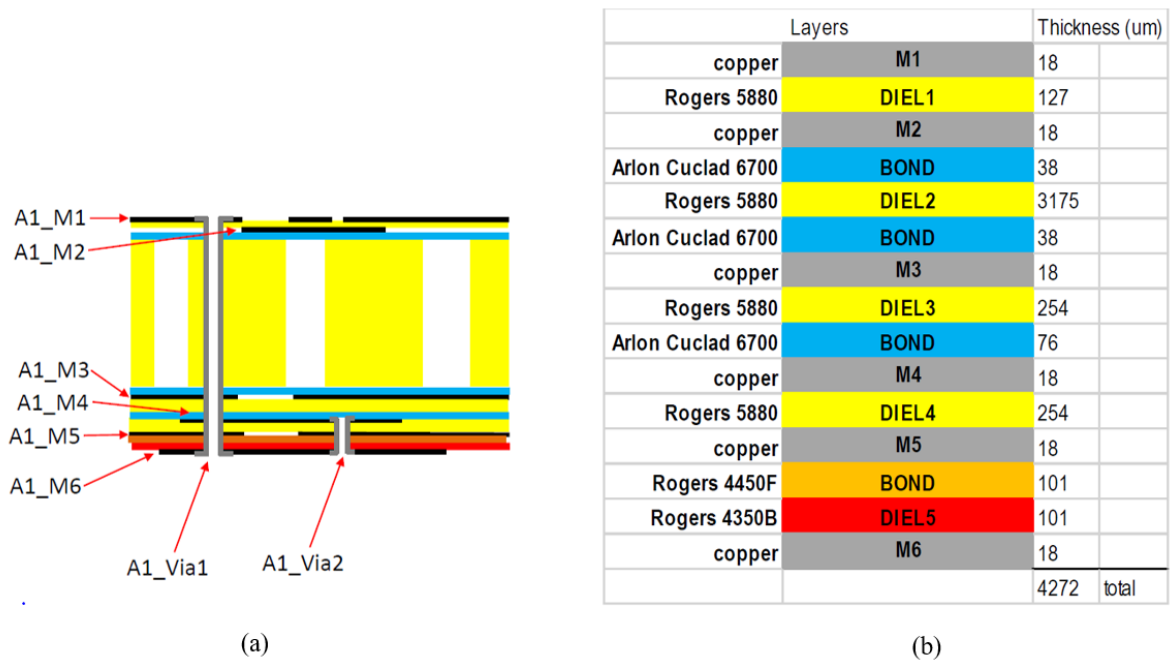


Figure B.2: Full stack-up of the 32×26 antenna board, including the layers thickness.

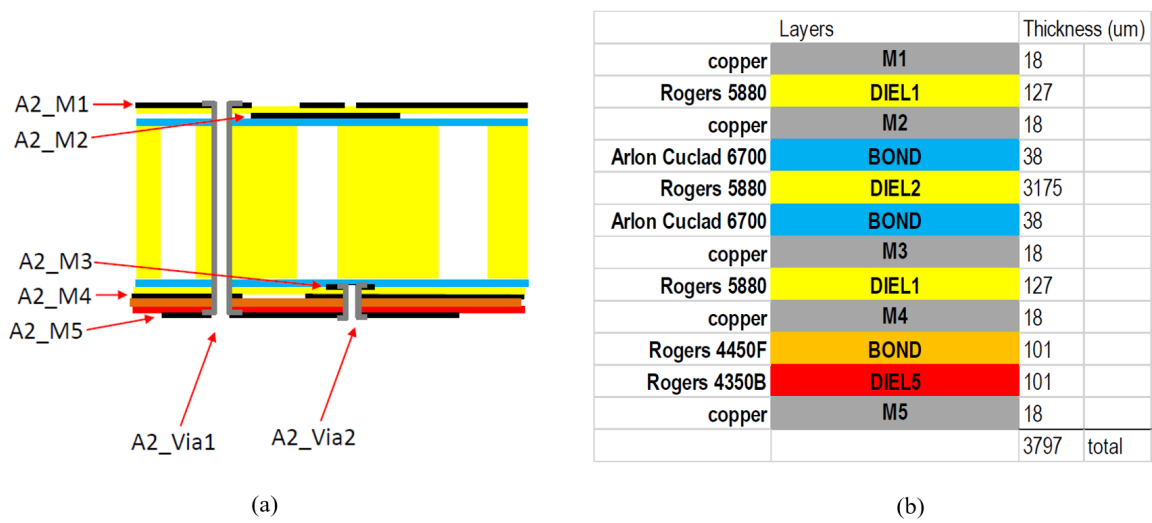


Figure B.3: Full stack-up of the 8x8 full connectorized antenna board, including the layers thickness.

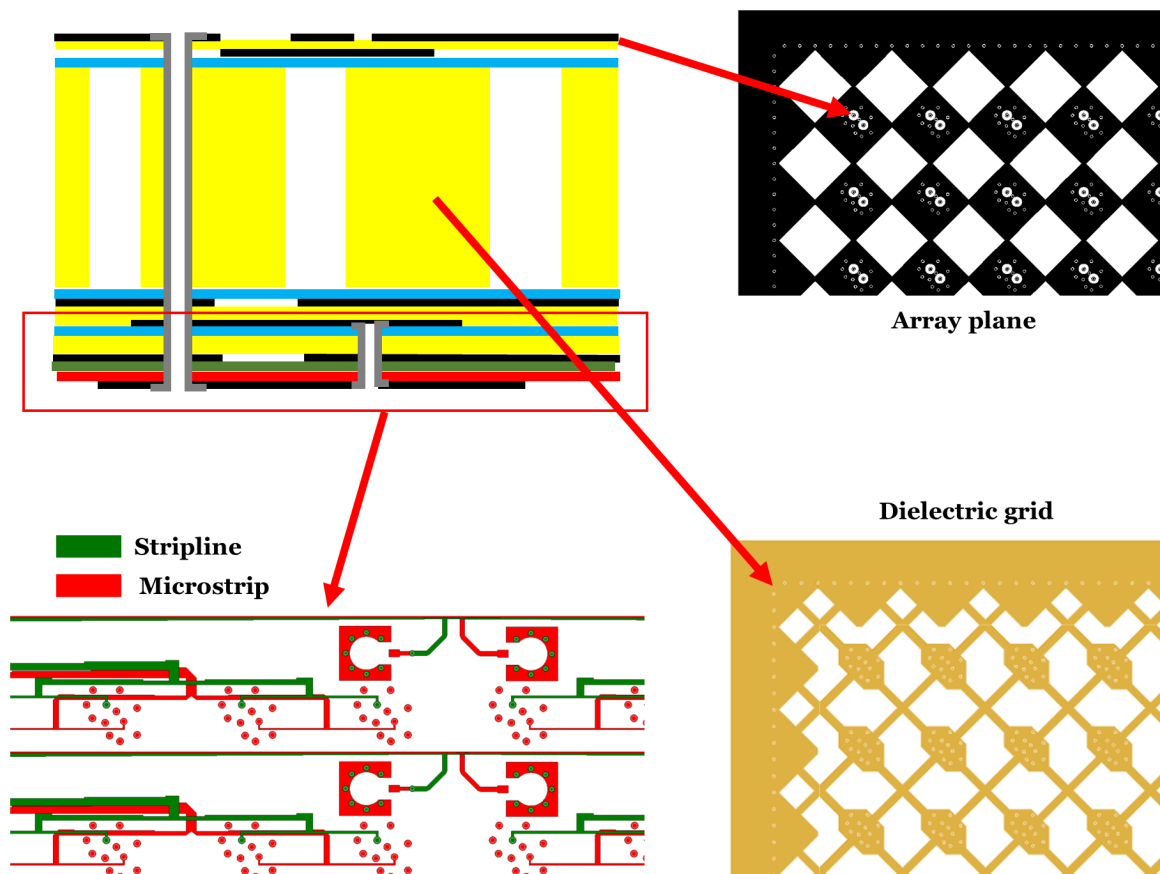
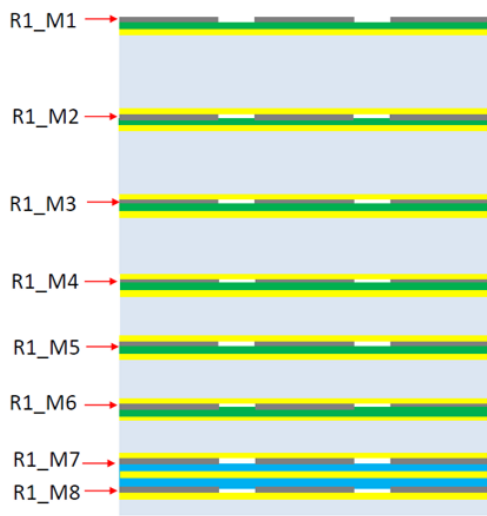


Figure B.4: 32x26 stack-up view with details from the array plane, the dielectric grid, and the feeding section.

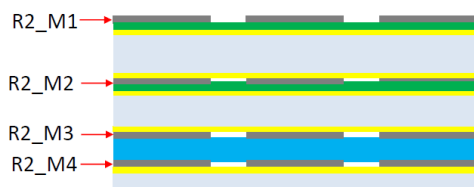


(a)

RADOME 1			
	Layers		Thickness (um)
copper	M1		18
DuPont Pyralux AP	DIEL1		25
Arlon CuClad 6250	BOND		38
Rohacell Foam			6572
Arlon CuClad 6250	BOND		38
copper	M2		18
DuPont Pyralux AP	DIEL1		25
Arlon CuClad 6250	BOND		38
Rohacell Foam			5650
Arlon CuClad 6250	BOND		38
copper	M3		18
DuPont Pyralux AP	DIEL1		25
Arlon CuClad 6250	BOND		38
Rohacell Foam			4803
Arlon CuClad 6250	BOND		38
copper	M4		18
DuPont Pyralux AP	DIEL1		25
Arlon CuClad 6250	BOND		38
Rohacell Foam			3388
Arlon CuClad 6250	BOND		38
copper	M5		18
DuPont Pyralux AP	DIEL1		25
Arlon CuClad 6250	BOND		38
Rohacell Foam			3150
Arlon CuClad 6250	BOND		38
copper	M6		18
DuPont Pyralux AP	DIEL1		25
Arlon CuClad 6250	BOND		38
Rohacell Foam			2719
Arlon CuClad 6250	BOND		38
copper	M6		18
Rogers 5880	DIEL2		381
Arlon CuClad 6250	BOND		38
Rogers 5880	DIEL2		1575
Arlon CuClad 6250	BOND		38
Rohacell Foam			500
			29546 Total

(b)

Figure B.5: Full stack-up of the WB ADL board and dielectric layers thickness.



Layers		Thickness (um)
copper	M1	18
DuPont Pyralux AP	DIEL1	25
Arlon CuClad 6250	BOND	38
Rohacell Foam		3379
Arlon CuClad 6250	BOND	38
copper	M2	18
DuPont Pyralux AP	DIEL1	25
Arlon CuClad 6250	BOND	38
Rohacell Foam		2403
Arlon CuClad 6250	BOND	38
copper	M3	18
Rogers 5880	DIEL2	1575
copper	M4	18
Arlon CuClad 6250	BOND	38
Rohacell Foam		766
		8435 Total

Figure B.6: Full stack-up of the NB ADL board and dielectric layers thickness.

Bibliography

- [1] E. G. Larsson, O. Edfors, F. Tufvesson, and T. L. Marzetta, “Massive MIMO for next generation wireless systems,” *IEEE Communications Magazine*, vol. 52, no. 2, pp. 186–195, 2014.
- [2] E. Bjornson, L. Van der Perre, S. Buzzi, and E. G. Larsson, “Massive MIMO in sub-6 GHz and mmWave: Physical, practical, and use-case differences,” *IEEE Wireless Communications*, vol. 26, no. 2, pp. 100–108, 2019.
- [3] W. Hong, Z. H. Jiang, C. Yu, J. Zhou, P. Chen, Z. Yu, H. Zhang, B. Yang, X. Pang, M. Jiang, Y. Cheng, M. K. T. Al-Nuaimi, Y. Zhang, J. Chen, and S. He, “Multibeam antenna technologies for 5G wireless communications,” *IEEE Transactions on Antennas and Propagation*, vol. 65, no. 12, pp. 6231–6249, 2017.
- [4] R. I.-R. F384-11, “Radio-frequency channel arrangements for medium- and high-capacity digital fixed wireless systems operating in the 6 425-7 125 mhz band,” Mar. 2012.
- [5] Y. Li, Z. Zhao, Z. Tang, and Y. Yin, “Differentially fed, dual-band dual-polarized filtering antenna with high selectivity for 5G Sub-6 GHz base station applications,” *IEEE Transactions on Antennas and Propagation*, vol. 68, no. 4, pp. 3231–3236, 2020.
- [6] Y. He, C. Li, and J. Yang, “A low-profile dual-polarized stacked patch antenna for micro-base-station applications,” in *2018 IEEE MTT-S International Wireless Symposium (IWS)*, 2018, pp. 1–4.
- [7] R. Cao, C. Y. D. Sim, and J. H. Zhuang, “A dual band dual-polarized sub-6GHz base station antenna,” in *2021 15th European Conference on Antennas and Propagation (EuCAP)*, 2021, pp. 1–4.
- [8] M. H. Novak, F. A. Miranda, and J. L. Volakis, “Ultra-wideband phased array for millimeter-wave ISM and 5G bands, realized in PCB,” *IEEE Transactions on Antennas and Propagation*, vol. 66, no. 12, pp. 6930–6938, 2018.
- [9] Y. Wang, L. Zhu, H. Wang, Y. Luo, and G. Yang, “A compact, scanning tightly coupled dipole array with parasitic strips for next-generation wireless applications,” *IEEE Antennas and Wireless Propagation Letters*, vol. 17, no. 4, pp. 534–537, 2018.
- [10] P. Gibson, “The Vivaldi aerial,” in *1979 9th European Microwave Conference*, 1979, pp. 101–105.
- [11] D. Schaubert, J. Shin, and G. Wunsch, “Characteristics of single-polarized phased array of tapered slot antennas,” in *Proceedings of International Symposium on Phased Array Systems and Technology*, 1996, pp. 102–106.

- [12] T.-H. Chio and D. Schaubert, "Parameter study and design of wide-band widescan dual-polarized tapered slot antenna arrays," *IEEE Transactions on Antennas and Propagation*, vol. 48, no. 6, pp. 879–886, 2000.
- [13] D. Schaubert, A. Boryssenko, A. van Ardenne, J. Bij de Vaate, and C. Craeye, "The square kilometer array (SKA) antenna," in *IEEE International Symposium on Phased Array Systems and Technology, 2003.*, 2003, pp. 351–358.
- [14] D. Schaubert, S. Kasturi, A. Boryssenko, and W. Elsallal, "Vivaldi antenna arrays for wide bandwidth and electronic scanning," in *The Second European Conference on Antennas and Propagation, EuCAP 2007*, 2007, pp. 1–6.
- [15] M. V. Ivashina, M. N. M. Kehn, P.-S. Kildal, and R. Maaskant, "Decoupling efficiency of a wideband vivaldi focal plane array feeding a reflector antenna," *IEEE Transactions on Antennas and Propagation*, vol. 57, no. 2, pp. 373–382, 2009.
- [16] J. Lee, S. Livingston, and R. Koenig, "A low-profile wide-band (5:1) dual-pol array," *IEEE Antennas and Wireless Propagation Letters*, vol. 2, pp. 46–49, 2003.
- [17] B. Munk, R. Taylor, T. Durharn, W. Crosswell, B. Pigon, R. Boozer, S. Brown, M. Jones, J. Pryor, S. Ortiz, J. Rawnick, K. Krebs, M. Vanstrum, G. Gothard, and D. Wiebelt, "A low-profile broadband phased array antenna," in *IEEE Antennas and Propagation Society International Symposium. Digest. Held in conjunction with: USNC/CNC/URSI North American Radio Sci. Meeting (Cat. No.03CH37450)*, vol. 2, 2003, pp. 448–451 vol.2.
- [18] Y. Zhou, F. Zhu, S. Gao, Q. Luo, L.-H. Wen, Q. Wang, X. Yang, Y. Geng, and Z. Cheng, "Tightly coupled array antennas for ultra-wideband wireless systems," *IEEE Access*, vol. 6, pp. 61 851–61 866, 2018.
- [19] L. Zhang, S. Gao, Q. Luo, W. Li, Y. He, and Q. Li, "A wideband circularly polarized tightly coupled array," *IEEE Transactions on Antennas and Propagation*, vol. 66, no. 11, pp. 6382–6387, 2018.
- [20] H. Zhang, S. Yang, Y. Chen, J. Guo, and Z. Nie, "Wideband dual-polarized linear array of tightly coupled elements," *IEEE Transactions on Antennas and Propagation*, vol. 66, no. 1, pp. 476–480, 2018.
- [21] S. Xiao, S. Yang, Y. Chen, S.-W. Qu, and J. Hu, "An ultra-wideband tightly coupled dipole array co-designed with low scattering characteristics," *IEEE Transactions on Antennas and Propagation*, vol. 67, no. 1, pp. 676–680, 2019.
- [22] Z. Zhang, S. Yang, J. Huang, S. Xiao, Y. Chen, and S. Qu, "Wideband tightly coupled dipole arrays with balanced scattering and radiation based on a black-box method," *IEEE Access*, vol. 7, pp. 118 402–118 410, 2019.
- [23] J. P. Doane, K. Sertel, and J. L. Volakis, "A wideband, wide scanning tightly coupled dipole array with integrated balun (tcda-ib)," *IEEE Transactions on Antennas and Propagation*, vol. 61, no. 9, pp. 4538–4548, 2013.

- [24] W. F. Moulder, K. Sertel, and J. L. Volakis, "Ultrawideband superstrate-enhanced substrate-loaded array with integrated feed," *IEEE Transactions on Antennas and Propagation*, vol. 61, no. 11, pp. 5802–5807, 2013.
- [25] M. H. Novak and J. L. Volakis, "Ultrawideband antennas for multiband satellite communications at UHF–Ku frequencies," *IEEE Transactions on Antennas and Propagation*, vol. 63, no. 4, pp. 1334–1341, 2015.
- [26] Y.-S. Kim and K. Yngvesson, "Characterization of tapered slot antenna feeds and feed arrays," *IEEE Transactions on Antennas and Propagation*, vol. 38, no. 10, pp. 1559–1564, 1990.
- [27] D. McGrath, N. Schuneman, T. Shively, and J. Irion, "Polarization properties of scanning arrays," in *IEEE International Symposium on Phased Array Systems and Technology, 2003.*, 2003, pp. 295–299.
- [28] S. M. Moghaddam, J. Yang, and A. U. Zaman, "Fully-planar ultrawideband tightly-coupled array (FPU-TCA) with integrated feed for wide-scanning millimeter-wave applications," *IEEE Transactions on Antennas and Propagation*, vol. 68, no. 9, pp. 6591–6601, 2020.
- [29] T.-L. Zhang, L. Chen, S. M. Moghaddam, A. U. Zaman, and J. Yang, "Millimeter-wave ultrawideband circularly polarized planar array antenna using Bold-C spiral elements with concept of tightly coupled array," *IEEE Transactions on Antennas and Propagation*, vol. 69, no. 4, pp. 2013–2022, 2021.
- [30] A. Neto and J. Lee, "'Infinite bandwidth' long slot array antenna," *IEEE Antennas and Wireless Propagation Letters*, vol. 4, pp. 75–78, 2005.
- [31] H. Wheeler, "Simple relations derived from a phased-array antenna made of an infinite current sheet," *IEEE Transactions on Antennas and Propagation*, vol. 13, no. 4, pp. 506–514, 1965.
- [32] D. Cavallo, W. H. Syed, and A. Neto, "Closed-form analysis of artificial dielectric layers—part I: Properties of a single layer under plane-wave incidence," *IEEE Transactions on Antennas and Propagation*, vol. 62, no. 12, pp. 6256–6264, 2014.
- [33] —, "Closed-form analysis of artificial dielectric layers—part II: Extension to multiple layers and arbitrary illumination," *IEEE Transactions on Antennas and Propagation*, vol. 62, no. 12, pp. 6265–6273, 2014.
- [34] D. Cavallo and C. Felita, "Analytical formulas for artificial dielectrics with nonaligned layers," *IEEE Transactions on Antennas and Propagation*, vol. 65, no. 10, pp. 5303–5311, 2017.
- [35] D. Cavallo and R. M. van Schelven, "Closed-form analysis of artificial dielectric layers with non-periodic characteristics," in *2019 13th European Conference on Antennas and Propagation (EuCAP)*, 2019, pp. 1–5.
- [36] W. E. Kock, "Metallic delay lenses," *The Bell System Technical Journal*, vol. 27, no. 1, pp. 58–82, 1948.

- [37] W. H. Syed, D. Cavallo, H. Thippur Shivamurthy, and A. Neto, "Wideband, wide-scan planar array of connected slots loaded with artificial dielectric superstrates," *IEEE Transactions on Antennas and Propagation*, vol. 64, no. 2, pp. 543–553, 2016.
- [38] D. Cavallo, W. H. Syed, and A. Neto, "Connected-slot array with artificial dielectrics: A 6 to 15 GHz dual-pol wide-scan prototype," *IEEE Transactions on Antennas and Propagation*, vol. 66, no. 6, pp. 3201–3206, 2018.
- [39] A. Van Katwijk and D. Cavallo, "Analysis and design of connected slot arrays with artificial dielectrics," in *2019 IEEE International Symposium on Phased Array System Technology (PAST)*, 2019, pp. 1–5.
- [40] D. Cavallo, W. H. Syed, and A. Neto, "6–15 GHz wide scanning connected array," in *2018 IEEE International Symposium on Antennas and Propagation USNC/URSI National Radio Science Meeting*, 2018, pp. 2155–2156.
- [41] V. Trainotti and W. G. Fano, "Overhead quasi-coaxial transmission lines," *IEEE Antennas and Propagation Magazine*, vol. 51, no. 6, pp. 93–101, 2009.
- [42] R. M. van Schelven, D. Cavallo, and A. Neto, "Equivalent circuit models of finite slot antennas," *IEEE Transactions on Antennas and Propagation*, vol. 67, no. 7, pp. 4367–4376, 2019.
- [43] D. Cavallo, R. Ozzola, N. Neto, and U. Imberg, "Requirement review," TU Delft, Tech. Rep. YBN2020045031, 2020.
- [44] D. M. Pozar, *Microwave Engineering; 3rd ed.* Hoboken, NJ: Wiley, 2005.
- [45] R. E. Collin, *Foundations for Microwave Engineering.* Wiley-IEEE Press, 2001.
- [46] L. Eriksson and B. As, "A high performance automotive radar for automatic AICC," in *Proceedings International Radar Conference*, 1995, pp. 380–385.
- [47] P. Herrero and J. Schoebel, "Planar antenna array at D-band fed by rectangular waveguide for future automotive radar systems," in *2008 38th European Microwave Conference*, 2008, pp. 1030–1033.
- [48] C. Felita and D. Cavallo, "Analytical tool for artificial dielectric layers (ADL GUI)," 2016. [Online]. Available: <http://terahertz.tudelft.nl/Research/project.php?id=114&pid=81>